Study of Pressure-Induced Halide Double Perovskite, $Cs_2LiGaBr_6$, For Photovoltaic Applications

By
Wajiha Tarannum Chaudhry
17311001

A thesis submitted to the Department of Mathematics and Natural Sciences in partial fulfillment of the requirements for the degree of
Bachelor of Science in Physics

Department of Mathematics and Natural Sciences
BRAC UNIVERSITY
July 2024

Declaration

It is hereby declare that

1. The thesis submitted is my own original work while completing degree at BRAC University.
2. The thesis does not contain material previously published or written by a third party, except where this is appropriately cited through full and accurate referencing.
3. The thesis does not contain material which has been accepted, or submitted, for any other degree or diploma at a university or other institution.
4. I have acknowledged all main sources of help.

Wajiha Tarannum Chaudhry
17311001

Approval

The thesis titled "**Study of Pressure-Induced Halide Double Perovskite, $Cs_2LiGaBr_6$, for Photovoltaic Applications**" submitted by **Wajiha Tarannum Chaudhry**, ID: 17311001, of Summer 2017, has been accepted as satisfactory in partial fulfillment of the requirement for the degree of **Bachelor of Science, Physics** on 10 July, 2024.

Examining Committee:

Supervisor:

_____

Dr. Md. Firoze H. Haque
Associate Professor, MNS
BRAC University

Co-Supervisor:

_____

Muhammad Lutfor Rahman
Assistant Professor, MNS
BRAC University

Program Coordinator:

_____

Muhammad Lutfor Rahman
Assistant Professor, MNS
BRAC University

Departmental Head:

_____

Dr. Md. Firoze H. Haque
Chairperson, MNS
BRAC University

Ethics Statement

To the best of my knowledge, this present study is the first theoretical exploration to demonstrate the pressure induced $Cs_2LiGaBr_6$ samples being suitable for photovoltaic applications. This material exhibits exceptional optical absorption and conductivity properties in the ultraviolet region of the electromagnetic spectrum.

I would like to declare that there are no known competing financial interest nor personal relationships which could have appeared to influence the work reported on this thesis.

Abstract

The production of lead-free halide double perovskites with visible spectrum bandgaps is an important advancement in the design of sustainable perovskite solar cells. In this study, DFT (Density Functional Theory) is used to examine the structural, optical, electrical, and mechanical characteristics of the lead-free $Cs_2LiGaBr_6$ double halide perovskites under hydrostatic pressure ranging from 2 GPa to 80 GPa. A decrease in the lattice constant is the result of increasing pressure. Direct band gaps are present in all $Cs_2LiGaBr_6$ compounds which progressively become wider under pressure. Changes in quantum confinement effects that are caused by compressive strain are largely responsible for the band gap variations under pressure. An examination of the optical characteristics and density of states indicates increased absorption in the visible band for the UV spectrum under pressure. The mechanical stability research highlights the compound's viability for thin-film fabrication by confirming its ductile character under pressure. This study highlights the potential of $Cs_2LiGaBr_6$ in a variety of settings and expands the knowledge of sustainable substitutes for perovskite optoelectronic applications.

Keywords:

Density Functional Theory; Double Halide Perovskites; Optical Properties; Electronic Properties; Mechanical Properties; Structural Properties.

Dedication

To

My father, Shafqat Rizwan Chaudhry

And my mother, Ishrat Chaudhry

Who have been constantly sacrificing and supporting from the beginning of my life to give me a bright future.

Acknowledgement

All praise to the Almighty for giving me strength, courage and patience to complete my thesis.

I would like to express my profound respect and gratitude to my supervisors Professor Dr. Firoze Haque and Assistant Professor Muhammad Lutfor Rahman, for their scholastic supervision, guidance and encouragement throughout the progress of this work.

I would like to convey my sincere gratitude to Professor Dr. A F M Yusuf Haider, Mehedi Hasan (City University), and the whole faculty of the Department of Mathematics and Natural Science, BRAC University for their kind assistance. I also appreciate the joint effort of the faculty of BRAC University's Department of Mathematics and Natural Science.

I want to thank everyone in my family and friends for their well wishes. Last but not least, I would like to include my parents and my devoted sister, who have sacrificed much since the beginning of my existence to see my happy face. I find it extremely difficult to put my love for them into words that would be enough.

Wajiha Tarannum Chaudhry

Table of Contents

List of Tables

List of Figures

List of Acronyms

XC	Exchange Correlation
VB	Valence Band
VRH	Voigt-Reuss-Hill
TDOS	Total Density of States
PDOS	Partial Density of States
PBE	Perdew-Burke-Ernzerhof
LDA	Local Density Approximation
KS	Kohn and Sham
HF	Hartree-Fock
GPa	Giga Pascal
GGA	Generalized Gradient Approximation
Fig.	Figure
eV	Electron Volt
EF	Fermi level
DOS	Density of States
DFT	Density Functional Theory
CB	Conduction Band
CASTEP	Cambridge Serial Total Energy Package
BO	Born-Oppenheimer
BFGS	Broyden-Fletcher-Goldfarb-Shanno
BZ	Brillouin Zone
Ab initio	from the beginning ("*ab initio*", Latin)

Chapter 1 Introduction

1.1 Background

The halide double-perovskite, also called elpasolites, constitute an extensive class of quaternary halides sharing the general formula $A_2^{1+} M^{2+} M^{3+} X_6^{1-}$ [1], [2]. Due to their Pb-free nature and potential for increased stability, a number of halide double-perovskite compounds, including $Cs_2AgBiCl_6$ and $Cs_2AgBiBr_6$, have been the focus of strong research efforts in materials science, especially with receiving attention for substitutes for the $CH_3NH_3PbI_3$ solar absorber material, with notable increase in their investigation in recent years [2], [3], [4]. Perovskites are widely acknowledged as a highly probable material to be used in next-generation solar cells, eventually replacing silicon [5], given their increasingly versatile nature, reduced cost and ease of fabrication methods. Perovskite cells' power conversion efficiency (PCE), which is certified at 25.8%, has improved rapidly. This is especially the case with tandem perovskite/CIGS (25%) and tandem perovskite/Si (monolithic) solar cells (33%) [5], [6], [7], [8].

For their use in high-efficiency solar cells, research has mostly been conducted on Methylammonium Lead Iodide ($CH_3NH_3PbI_3$), Cesium Lead Iodide ($CsPbI_3$), Formamidinium Lead Iodide ($FAPbI_3$) and Methylammonium Lead Bromide ($CH_3NH_3PbBr_3$) [10], [9], [10], [11]. Organo-halide perovskites are used in photovoltaics and light-emitting diodes (LEDs) because of their composition, which consists of natural, more affordable components and is versatile to support the range of processing methods, most notably the solution-based deposition techniques [12], [13], [14], [15]. While efficiency levels have been obtained making them cost-effective, there are still a number of obstacles to overcome, including large-scale manufacturing, moisture instability for outdoor operation, and the serious repercussions that compounds like lead (Pb) have for both the environment and human health [16], [17], [18], [19]. Perovskites are suitable tandem partners because they perform well in the regions of the spectrum where silicon PVs struggle [13], [20].

Simultaneously, the study of $Cs_2LiGaBr_6$ presents a novel contribution, integrating for the first time the Generalized-Gradient-Approximation (GGA) and Perdew-Burke-Ernzerhof (PBE) techniques. The widely used computational method GGA-PBE provides new insight into the pressure-induced characteristics of $Cs_2LiGaBr_6$, increasing our understanding of environmentally friendly perovskite materials [21]. The broader scientific discussion on sustainable perovskite materials is greatly enhanced by this investigation. The fact that $Cs_2LiGaBr_6$ has bandgaps in the visible range adds relevance to the material and represents a significant breakthrough in the creation of eco-friendly perovskite solar cells. The detailed examination includes the mechanical, optical, electrical, and structural characteristics of $Cs_2LiGaBr_6$, on the effects of hydrostatic pressure in the range of 2 GPa to 80 GPa. The hydrostatic pressure demonstrated tunable bandgap and enhanced optical absorption behavior to lattice parameters, which had substantial impact on $Cs_2LiGaBr_6$'s optical and mechanical properties [22], [23], [24]. The pursuit for lead-free metal-halide perovskites that function like their conventional lead-based counterparts is an important scientific goal in the larger framework of modern research. This work contributes to the growing understanding of $Cs_2LiGaBr_6$ under various settings and furthers the overall objective of developing environmentally acceptable solar application options.

1.2 Objectives of the Present Study

The aim of this research proposal is to investigate the different physical characteristics of pressure-induced $Cs_2LiGaBr_6$ for applications in high-performance photovoltaic devices.

Using DFT, the following tasks are completed:

- Examining the structural characteristics.
- Examination of mechanical characteristics, including Pugh's ratio, Poisson's ratio, Young's modulus, Shear modulus, and Bulk modulus.
- Research on electronic characteristics, such as band structure and state density.
- Examining the optical functions (dielectric constant, absorbance, conductivity, and reflectivity).

- Examination of how pressure affects the different physical characteristics of the metal halide $Cs_2LiGaBr_6$.

1.3 Outline of the Thesis

The following structure applies for the thesis:

- The theory of the literature review and the properties that were looked into are presented in Chapter 2.
- The basic theoretical approaches related to the first-principle computations are covered in Chapter 3.
- Results and a detailed explanation of the various physical parameters examined in the investigation are presented in Chapter 4.
- The last observation and the range of further work are presented in Chapter 5.

Chapter 2 Literature Review and Theory of Investigated Properties

2.1 Literature Review

Using the CASTEP algorithm, this paper explores the intricate modeling of $Cs_2LiGaBr_6$, a novel lead-free double halide perovskite. The hunt for environmentally benign substitutes in perovskite materials has been ongoing in the recent few decades [6], [25], [12], [26], [27], [28], [29]. Significant research has been done on the band gap characteristics of lead-free halide double perovskites ($Cs_2BiAgCl_6$ and $Cs_2BiAgBr_6$) and novel semiconductors (Cs_2AgBiX_6, X = Br, Cl), respectively, by Filip et al. and McClure et al. [30], [4]. Cs_2AgBiX_6 (X= Cl, Br, and I) was studied by Chrafih et al. for solar cell applications [31]. S. Amraoui et al. used a solar cell capacitance simulator (SCAPS) to simulate a double perovskite based photovoltaic cell [25]. Saeed et al. investigated the band gap and stability of $Cs_2NaGaBr_6$ and $Cs_2LiGaBr_6$ in the presence of SOC + mBJ [32]. Furthermore, the potential of lead-free halide double perovskites (Cs_2CuMCl_6, M = Sb, Bi) for green technology was investigated by Nabi et al [33]. The effects of internal and external pressure on cubic perovskites, such as $CsSnCl_3$, are evaluated by Metin et al. [34]. Together with other inorganic halide perovskites, Ying et al. revealed the tunable optical characteristics phase of $CsSnCl_3$ under pressure [35]. In addition, the present work uses DFT to thoroughly examine the impacts of different hydrostatic pressures on the mechanical, electrical, optical, and structural characteristics of $Cs_2LiGaBr_6$ metal halide. These initiatives demonstrate a shared dedication to lead-free perovskite and represent progress in the direction of sustainability.

2.2 Fundamental Characteristics of Crystal

The crystal structure describes the periodic arrangement of atoms, ions, or molecules in a crystalline substance. Periodicity is the essential characteristic of the crystal structure. The material's elastic, mechanical, optical, and other characteristics are greatly influenced by the periodic arrangement of its atoms. The arrangement of atoms within a material allows for the classification of the material into two categories (crystalline and amorphous). Crystalline materials are made up of atoms or molecules organized in an ordered and regular structure (NaCl, CsCl, etc.). Conversely, materials that are non-crystalline or amorphous have atoms or molecules organized in a way that prevents their positions from being periodic (Polyvinyl chloride, Fiber-glass, Naphthalene, etc.). Polycrystalline materials, including most crystal materials, are composed of millions of individual crystals known as grains that vary in size and orientation. The majority of inorganic materials, like most rocks and ceramics, are the common polycrystalline materials. The lattice and basis combine to generate the crystal structure. A regular and well-organized arrangement of points in space is called a lattice. The crystal structure develops when an atomic basis is uniformly bonded to every lattice point, where the basis is the number of atoms or molecules at the lattice point. The collection of atoms with equivalent composition, arrangement, and orientation is defined by the basis. This chapter aims to provide readers with a thorough understanding of the crystal structure of $Cs_2LiGaBr_6$ and its many structural parameters, as well as an outline of the theory used to explore the structural, electrical, optical, and mechanical properties of this perovskite-type semiconductor.

2.3 Crystal Structure of $Cs_2LiGaBr_6$

2.3.1 Unit cell

The cubic $Fm\bar{3}m$ space group is exhibited by the pristine crystal structure of the cubic $Cs_2LiGaBr_6$ perovskite. Distinct atomic positions are defined inside its unit cell as follows: at the 8c Wyckoff site, Cs atoms are positioned face-centered and are identified by fractional coordinates (0.25, 0.25, 0.25); Ga atoms are located at the body-centered site in the 4b Wyckoff site, with fractional coordinates of (0.5, 0.5, 0.5); Li atoms are placed at the corner positions in the 4a Wyckoff site, with fractional coordinates of (0, 0, 0);

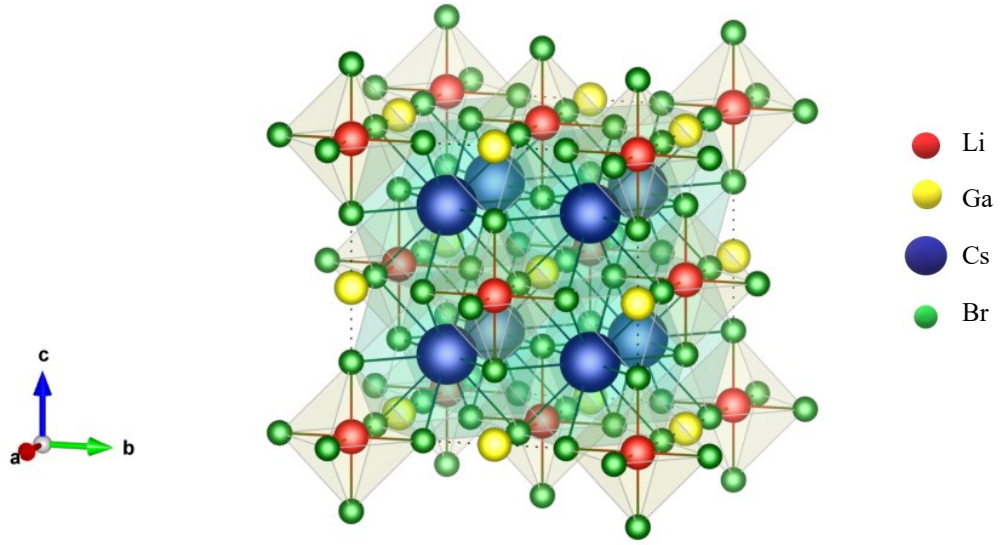

Figure 1: The constructed unit cell of $Cs_2LiGaBr_6$ double perovskite.

and Br atoms are face-centered in the 24e Wyckoff site, with fractional coordinates of (0.2513, 0, 0).

The cubic crystal structure of the $Cs_2LiGaBr_6$ unit cell is shown in **Figure 1**. The figure shows the crystal structure of $Cs_2LiGaBr_6$ as shown by VESTA (Visualization for Electronic and Structural Analysis) [36]. CsBr cuboctahedra are created when the Cs^{3+} makes bonds with twelve equivalent Br^{3-} atoms. These cuboctahedra are comparable to CsBr cuboctahedra, LiBr octahedra, and GaBr octahedra. They also share corners, faces, and edges. A total of 40 atoms, distributed as follows, were produced by building a 1×1×1 supercell: 8 Cs, 4 Li, 4 Ga, and 24 Br atoms.

2.3.2 Lattice parameters

The lattice parameters of a three-dimensional crystal lattice are defined as the angles along each crystallographic axis, denoted by α, β, and γ; the cell edge lengths are denoted as a, b, and c. The vector "b" and the vector "c" have an angle of α, whereas the vectors "c and a" and "a and b" have angles of β and γ, respectively. The lattice parameters define the separations between the closest atoms in a crystal. In actuality, the unit cells' physical dimensions in a crystal lattice are described by the lattice parameters. The connection between the initial lattice parameters in $Cs_2LiGaBr_6$ is $a = b = c$ = 10.937137 Å and $\alpha = \beta = \gamma$ = 90° [37].

2.3.3 Unit cell volume

The dot product combining a single vector by a cross product of corresponding two vectors yields the volume (V), of a unit cell given by: $V=\boldsymbol{a}\cdot(\boldsymbol{b}\times\boldsymbol{c})$, where the lengths of the cell edges of the unit cell are represented by the vectors a, b, and c and their inter-axial angles by α, β, and γ. The following formula is used to determine the unit cell's volume:

$$V = abc[\sqrt{1} - cos^2\alpha - cos^2\beta - cos^2\gamma + 2cos\alpha cos\beta cos\gamma] \quad \ldots(1)$$

When the inter-axial angles are expressed as $\alpha=\beta=\gamma=90°$ and the edge lengths as $a=b=c$, the unit cell's volume is expressed as

$$V = a^3 \quad \ldots(2)$$

The volume of the cubic crystal $Cs_2LiGaBr_6$ is obtained by,

V = 1308.311023 $Å^3$ for cubic $Cs_2LiGaBr_6$.

2.4 First-Principles Computational Details

The CASTEP algorithm was applied in the research to conduct first-principles calculations. The exchange-correlation energy was obtained by using the Perdew-Burke-Ernzerhof function and Generalized Gradient Approximation (PBE-GGA). The $Cs_2LiGaBr_6$'s crystal structure was optimized by the Limited-memory Broyden-Fletcher-Goldfarb-Shanno (L-BFGS) minimization technique. The Brillouin zone (BZ) specific k-point sampling was enabled by the Monkhorst-Pack technique.

A 500 eV plane wave cutoff energy, and the 3×3×3 k-points were used for a single unit cell of $Cs_2LiGaBr_6$, providing convergence tolerances: maximum force on atoms at 0.01 eV/é, energy at 5.0×10^{-6} eV/atom, maximum atomic displacement set at 5.0×10-4Å and maximum stress of 0.02 GPa, during structure optimization, while analyzing the optical, structural and electronic properties of the material. The calculated C_{ij} values from the CASTEP module were used in the Voigt-Reuss-Hill (VRH) averaging technique to determine the mechanical characteristics. For this analysis, the maximum force applied to the atoms was set at 0.01 eV/e, the maximum displacement at 4.0×10^{-4}Å, and the energy at 4.0×10^{-6} eV/atom. These demanding conditions were selected to thoroughly analyze and precisely assess the material's characteristics.

2.4.1 Geometry Optimization

In CASTEP computations, geometry optimization plays a critical role in determining the molecule's minimal energy configuration. Many of a molecule's chemical and physical characteristics are determined by the optimization of its geometry. Thus, while doing computations, it is crucial to comprehend geometry optimization. In computational chemistry, optimization is our primary focus. On the potential energy surface, minima are found by geometry optimization; these minimal energy structures are equivalent to equilibrium structures. The position of transition structures is found through optimization; they are depicted

as saddle points on the potential energy surface. Energy minimization is an alternate term for optimization to minima. By changing the atomic coordinates, molecules' energy is decreased during reduction. Energy minimization is carried out when applying both quantum mechanical or molecular mechanical techniques, and it has to come before any computational studies that use these techniques.

Geometry optimization can be used to:

- describe the properties of a potential energy surface;
- obtain a structure for a calculation of single-point quantum mechanics that produces a wide range of electrical and structural features;
- Build a framework for the molecular dynamics simulation; if the forces acting on the atoms are too great, the integration algorithm might not work.

2.4.2 Optical Properties

The way a substance reacts to electromagnetic radiation defines its "optical properties". There are instances in which it is crucial to anticipate and monitor the reactions of radiations exposed to electromagnetic radiation. When we comprehend the mechanics underlying their optical behaviors and are acquainted with their optical qualities, this becomes feasible. A few fundamental theories and ideas about the nature of electromagnetic radiation and its potential interactions with solid objects will be covered in this part. In addition to the occupied and unoccupied states of the electrical structure, the band characteristics are also taken into account while calculating optical spectra. To gain a deeper understanding of the electrical structure of materials, it is therefore intriguing to investigate their optical characteristics.

Furthermore, the best technique to verify the estimated electrical structure is to compare the optical spectra with experimental data. The optical response of the medium is known to be described by the dielectric function $[\varepsilon(\omega) = \varepsilon_1(\omega) + i\varepsilon_2(\omega)]$ for all photon energy $E = \hbar\omega$. The dielectric $\varepsilon_2(\omega)$ imaginary

component can be computed by adding up the transitions between occupied and unoccupied states. In particular, the imaginary portion of the dielectric function $\varepsilon_2(\omega)$ is given by [38] in this study.

$$\varepsilon_2(\omega) = \frac{2e^2\pi}{\Omega\varepsilon_0}\Sigma_{k,v,c}|\psi_k^c|u.r|\psi_k^v|^2\delta(E_k^c - E_k^v - \hbar\omega) \quad \ldots(3)$$

Employing the Kramers-Kronig combination, the real component of the dielectric function may be separated from the imaginary part in the following way [39], [40]:

$$\varepsilon_1(\omega) = 1 + \frac{2}{\pi}P\int_0^\infty \frac{\omega'\varepsilon_2(\omega')d\omega'}{(\omega'^2 - \omega^2)} \quad \ldots(4)$$

Where, *P* implies the principal value of the integral.

Important optical functions may be calculated with the knowledge of the dielectric tensor's real and imaginary portions. In this work, we examine the optical conductivity *σ(ε),* the reflectivity *R(ω),* and the absorption coefficient *(ω).* The reflectivity spectra are obtained by applying the relation [41] to Fresnel's formula for normal incidence, assuming that the crystal surface is oriented parallel to the optical axis:

$$\mathrm{R}(\omega) = \left|\frac{\sqrt{\varepsilon(\omega)} - 1}{\sqrt{\varepsilon(\omega)} + 1}\right|^2 \quad \ldots(5)$$

All other optical parameters, including reflectivity *R(ω)* and absorption coefficient $\alpha(\omega)$, may be computed using $\varepsilon_1(\tau)$ and $\varepsilon_2(\omega)$ as their starting points [41], [42].

$$\mathrm{R}(\omega) = \left|\frac{\sqrt{\sqrt{\varepsilon_1(\omega) + \mathrm{j}\varepsilon_2(\omega)} - 1}}{\sqrt{\sqrt{\varepsilon_1(\omega) + \mathrm{j}\varepsilon_2(\omega)} + 1}}\right|^2 \quad \ldots(6)$$

$$\alpha\,(\omega) = \sqrt{2}(\omega)\left(\sqrt{\varepsilon_1(\omega)^2 + \varepsilon_2(\omega)^2}\right)^{\frac{1}{2}} \quad \ldots(7)$$

2.4.3 Electronic Properties

The electronic band structure, also known as the band structure of a solid, in solid-state physics denotes the energy ranges that an electron is "permissible" or "prohibited" to have. This results from the quantum mechanical electron's diffraction of waves in the periodic crystal lattice, which makes sense in light of quantum mechanics. By analyzing an electron's quantum mechanical wave function in a periodic lattice of solids, molecules, or atoms, the band theory is able to determine these band gaps and the bands. In a periodic crystal lattice, the quantum mechanical electron's diffraction of waves with a particular Bravais lattice and crystal system gives rise to band structure. A material's band structure influences a number of attributes, most notably its optical and electrical capabilities. Both the intramolecular and intermolecular bonding interactions are described in detail in the band structure diagram. One of the most important features of the band structure is the band-gap, which has a significant impact on the material's optical and electrical characteristics. By use of carrier production and recombination processes, electrons can move from one band to another. Semiconductor apparatus like diodes, solar cells, transistors, laser diodes, and others may be made using the band gap. Moreover for the individual atomic orbitals, the crystal structure and energy levels determine the band structure.

At a Brillouin zone, each state is identified by the wave number. For a big crystal, this wave number is stacked extremely densely near the Brillouin zone. An identified wave number's lowest-lying state is referred to as the first band, its next lowest-lying condition as the second band, and it continues. The bands and band gaps with energy close to the Fermi level (EF) are the most significant and important to electronics and optoelectronics.

Depending on the material, distinct designations are assigned to the bands and the band-gaps close to the EF:

- A band gap encloses the EF in a semiconductor, also known as the band insulator. The conduction band is the next closest band above the band gap, while the valence band is the closest band below the band gap. The valence band in many semiconductors is constructed of valence orbitals.
- The EF in a semimetal or metal is located inside one or more permitted bands. By analogy to semiconductors, the bands in semimetals are typically called "valence band" or "conduction band" based upon the fact how the charge transport is being more hole-like or electron-like.

As valence orbitals make up the bands in many metals, they are commonly referred to as "valence bands" despite being neither electron- or hole-like.

Since they are too distant from the EF, in low energy physics the band gaps present on the structure of a metal's band do not have much impact. The wave vectors of the energy states in a band gap can be used to categorize the energy band gaps [45]:

- Indirect band gap: the k values of the closest states above and below the band gap are different.
- Direct band gap: the energy states with the highest energy below the band gap and the lowest energy above it have the same k value.

The number of states per energy interval at each energy level that can be occupied is described by the density of states (DOS) of a system in solid-state and condensed matter physics. The density distributions are continuous rather than discrete, as in the case of isolated systems, including the molecules or atoms in the gaseous phase.

At a certain energy level, the high DOS denotes a significantly large number of states that are open for occupancy. There are no states that can be occupied at that energy level when the DOS is 0. For a fast visual inspection of the electrical structure, DOS is frequently utilized. Qualitative interpretation of the experimental spectroscopic data is aided by characteristics including the number and intensity of the principal features, the insulators' energy gap, and the breadth of the valence band. Understanding the alterations in electrical structure brought about by, say, external pressure, is another benefit of DOS analysis. Numerous numerical methods exist for assessing the DOS. Ackland [46] devised a reduced linear interpolation approach that is used by CASTEP.

This approach has its foundation on parallelepiped linear interpolation derived from the Monkhorst Pack set points, followed by sampling the resultant set of band energies from a histogram. In the partial density of states (PDOS) figure, only the valence band and the lower portion of the conduction band are significant. Similar to the total DOS computation, the computation itself can be performed using the linear interpolation or the Gaussian smearing. Counting the number of states in the system that have the energy in concern multiplied by the function of probability distribution, is required to get the real amount of electrons in a particular energy level. Thus, the $F(\mathscr{E})$ is the electrons functional probability in a particular energy state and $g(\mathscr{E})d\varepsilon$ is the total number of quantum states that are accessible in the energy range, and $\varepsilon + d\varepsilon$, is the actual number of electrons that are present in what is referred to as the free state in the energy range above at any temperature is given by

$$(\mathcal{E})\mathrm{d}\mathcal{E} = F(\mathcal{E})(\mathcal{E})\,\mathrm{d}\mathcal{E} \qquad \ldots(8)$$

where the density of states is denoted by the number $g(\mathscr{E})$. Naturally, there will be a difference between the quantum and classical values of $g(\mathscr{E})$. In general, the wide range of the amount of energy levels per eV versus energy is known as the density of states (DOS). A material's electronic structure can be understood qualitatively by utilizing the electronic density of states by considering the partial density of states (PDOS). According to the PDOS, the states are associated to the fundamental operations and then to the unit cell's atoms. Next, the sum over the atomic contributions represents the total DOS. The expression is used to compute the DOS.

$$n(\varepsilon) = 2\Sigma_{n,k}\delta(\varepsilon - \varepsilon_n^k) = \frac{2}{V_{BZ}}\Sigma_n\delta(\varepsilon - \varepsilon_n^k)dk \qquad \ldots(9)$$

where k is the integral over the BZ and δ is the Dirac delta function. The unit cell's electron number is determined by

$$\int_{-\infty}^{\varepsilon_F} n(\varepsilon)\mathrm{d}\varepsilon \qquad \ldots(10)$$

2.4.4 Elastic Properties

The Poisson's ratio, Young's, shear, and bulk moduli, are characteristic of how the crystals behave with relation to external forces. It is evident that the elastic constants have a significant role in determining the materials' strength. Before determining elastic constants, geometry optimization is not required to be done; C_{ij} data for the empirically observed structure can be obtained. On the other hand, full geometry optimization — which includes cell optimization — yields accurate results when the elastic constants are calculated for the structure that matches the theoretical ground state. Cubic $Cs_2LiGaBr_6$ has three separate components that make up its elasticity tensor. Additionally, the energy of the ground states second derivative with regard to the strain components *(i)* are specified as the independent elastic constants. In general, it may be expressed mathematically as,

$$C_{i,j} = \frac{1}{V}\left(\frac{\partial^2 E}{\partial \varepsilon_i \, \partial \varepsilon_j}\right) \qquad \ldots(11)$$

Where *E* stands for the unit cell's energy and *V* is the volume.

From the Taylor expansion of the total energy *E (V, δ)* for the system with regard to a tiny strain *δ* of the lattice primitive cell volume *V,* elastic constants are determined. The energy of a strained system is expressed as follows [45]:

$$E(V,\delta) = E\,(V_0, 0) + V_0\left[\Sigma_i \tau_i \xi_i\, \delta_i + \frac{1}{2}\Sigma_{i,j}\, C_{ij}\delta_i \xi_i \delta_j\right] \qquad \ldots(12)$$

Where the equilibrium volume of the energy of the unstrained system is represented by $E\ (Vo,\ 0)$. The variables V_o, τ_i, and δ_i are components of the stress tensor and factors that affect the Voigt index.

Three independent symmetry components $(C_{11}, C_{12}\ and\ C_{44})$ are identified in the cubic $Cs_2LiGaBr_6$, and they all correspond to elastic constants

$$(C_{11} = C_{22} = C_{33}; C_{12} = C_{21}, C_{12} = C_{23} = C_{31}; C_{44} = C_{55}\ and\ C_{66})\ .$$

One way to calculate the elastic constants of the initial principles is to set the strain or stress to a finite volume, calculate the strain or stress, respectively, then re-optimize any free parameters. Elastic constants can then be found by selecting the applied deformation carefully. However, because the unit cell is permanent and does not need to be optimized, implementing a specific homogeneous distortion (strain) and computing the associated stress often needs significantly lesser computational work. Several investigations have demonstrated that DFT elastic constant accuracy is usually between the experiments 10% or less. This enables us to forecast elastic constants for novel materials [47] or additional materials for which there are no experimental data; it also permits us to forecast elastic characteristics under pressure or unify inconsistent experimental findings. The following relations [48] are used to derive the Reuss and Voigt constraints of shear (G) and bulk (B) moduli for the cubic crystal:

$$B_v = B_R = \frac{C_{11} + 2C_{12}}{3} \quad \ldots(13)$$

$$G_v = \frac{C_{11} - C_{12} + 3C_{44}}{5} \quad \ldots(14)$$

$$G_R = \frac{5C_{44}(C_{11} - C_{12})}{[4C_{44} + 3(C_{11} - C_{12})]} \quad \ldots(15)$$

Using the values of B_v and G_R, the numerical values of G and B is calculated using the Hill's approximation as follows:

$$B = \frac{1}{2}(B_R + B_v) \quad \ldots(16)$$

$$G = \frac{1}{2}(G_v + G_R) \quad \ldots(17)$$

Poisson's ratio (v) and Young's modulus (E) are calculated by using the G and B as follows,

$$E = \frac{9GB}{3B + G} \quad \ldots(18)$$

$$V = \frac{3B - 2G}{2(3B + G)} \quad \ldots(19)$$

Chapter 3 Research Methodology

3.1 Classification of Methodology

The academic community has focused a great deal of effort in recent years on computer-based hypothetical simulations to identify the different characteristics of materials in the fields of Chemistry and Physics. Analytical investigations may not always yield the same results as computer-based theoretical computations, so to investigate the material's structure and determine its different characteristics, a number of techniques are employed. Three distinct types of methodologies may be identified: (i) the ab-initio or first principles method; (ii) the semi-empirical or empirical method; including (iii) the method of molecular mechanics.

Methods based on ab-initio or first principles does not need empirical data to be computed. The values of a few key parameters and the principles of quantum physics are the main sources of dependence for the ab-initio procedures. For calculating small molecular systems, ab-initio approaches may yield extremely precise results. Semi-empirical approaches, on the other hand, can perform calculations for macro molecules with less accuracy and require empirical data obtained through experimentation in order to simplify the calculations. Molecular mechanics techniques apply classical physics to the study of atom and molecular dynamics. This chapter mostly describes the ab-initio procedures. The first-principles or ab-initio approaches are helpful in forecasting the characteristics of novel materials. For example, they may be used to calculate the energy levels of solid-state electrons, as indicated by their energy bands, being the fundamental theoretical challenge in the solid-state of physics. Previously, the attainable size of systems for ab-initio approaches were severely limited. Nevertheless, the issue with the aforementioned two approaches has been that, in the absence of computers, the sheer amount of integrals that need to be assessed renders them unfeasible on actual systems. The ability to accurately calculate energies and related properties

for systems with up to twelve atoms, including the heaviest elements in the periodic table, in just a mere few minutes is made possible by the remarkable advancement of low-cost, powerful computers. Unlike previously mentioned techniques, ab-initio computations can yield excellent quantitative predictions over a wide range of the system. Thus, in order to study structural, electrical, optical, and mechanical characteristics, calculations were carried out throughout this research using an ab-initio plane wave pseudopotential approach inside the DFT framework employing GGA as used in CASTEP code [40]. This chapter provides an in-depth discussion of the complex mathematical processes involved in the ab-initio approaches.

3.2 The Wave Function

The probability of a particle quantum state as a function of time, position, momentum, and spin is expressed as a wave function. To represent the wave function, the symbol Ψ is used. In quantum physics, the wave function is an expression in mathematics that is used to characterize a particle system or quantum state. A wave function is simply described as one that explains the qualities of a wave and satisfies the wave equation. A probability function being a real number, is represented by the symbol $|\Psi|^2$, whereas a wave function is a complex number where locating the particle at a specific location and time has a probability of $|\Psi|^2$. For instance, the wave function of an electron fully describes the behavior of the electron in an atom with a lone electron, like a hydrogen or an ionized helium. The temporal evolution of a wave function is explained by the Schrödinger equation and the rules of quantum physics. As a mathematical form of wave equation, the Schrödinger equation causes the wave function to behave qualitatively like other waves, such as waves on a string or in water. This leads to wave-particle duality and defines the term wave function.

3.3 The Schrödinger Equation

The fundamental equation in physics used to analyze quantum mechanical activity is the Schrödinger equation. This partial differential equation, which describes the evolution of a physical system's wave function over time, is referred to by Schrödinger's wave equation. To find the energy levels of quantum mechanical systems, one applies the Schrödinger equation. The time-independent and the time-dependent Schrödinger equations are two separate equations that are generally referred to as the "Schrödinger equation". The time-independent Schrödinger equation is the foundation of both the wave function mechanics and the DFT (density functional theory) [49],

$$\widehat{H}\Psi = E\psi \qquad \ldots(20)$$

Where the total energy, E, of the system and H is the Hamiltonian operator that acts on to provide its eigenvalue. Other operators are accessible as well, such as spin and electric dipole moments. For the physical observables, these may be utilized to get the wave function's expectation values. The Schrödinger equation is challenging to solve for non-hydrogenic systems without approximations, despite its apparent simplicity. The Born-Oppenheimer (BO) approximation is the fundamental approximation which separates the motion of the system's electrons from that of its nuclei. According to the Born-Oppenheimer approximation, any modification to the nuclei's positions results in an instantaneous restructuring of the electronic configuration; in other words, the nuclei are seen as fixed with regard to the motion of electrons at any geometry, making it easier to assess the interactions between the nuclei and the nuclear kinetic energy, the electron-nucleus, and the nucleus-nucleus. An interpretation of the approximation is that when the nuclei move, electrons immediately realign because of the enormous mass differential between them and the nucleus.

$$(H_{el} + V_N)\Psi = E_{el}\psi_{el} \qquad \ldots(21)$$

$$H_{el} = T_s + V_{en} + V_{es} \qquad \ldots(22)$$

The nuclear-nuclear interactions (V_N) and the electronic interactions (H_{el}) make up the operators in the electronic Schrödinger equation (21). In equation (22), H_{el} is made up of the electrons' kinetic energy, T_e; electron-electron potential energy, V_{en}; and electron-nuclear potential energy, V_{es}. The BO approximation states that V_N is a constant at every geometry, therefore it may be inserted as a parameter and subtracted from the equation. Almost all quantum chemistry programs solve the electronic Schrödinger equation.

3.4 Pseudopotentials

A pseudopotential is built with the core radius, r_c, so that it demonstrates symmetry with the actual potential outside of that radius. The ab-initio method is used to build the pseudopotential. The purpose of the pseudopotential is to provide an effective potential, or pseudopotential, for the non-valence electrons in an atom with its nucleus in place of the Columbic potential factor, which is generally contained in the Schrödinger equation. This enables for a modified effective potential term to be included in the equation instead of the Columbic potential term.

Beyond this distance, each pseudo wave function has to align with the appropriate true wavefunction. It is also necessary for the charge densities obtained outside of the core area to match the actual charge density. As a result, over the core region, the integral of the squared amplitudes of the actual and pseudo wave functions must match. Norm-conservation is the name given to this circumstance [43]. Phase changes during scattering over the core must be retained, along with all other atomic characteristics of the element. Since these phase shifts will vary depending on the angular momentum state, the pseudopotential must generally be non-local and have projectors for the various angular momentum components. Hans Hellmann initially presented the pseudopotential approximation in the 1930s. Using a plane wave basis set, the computational complexity would still be prohibitive even if every electron in the system were explicitly included in the calculation and built from the whole Columbic potential of the nucleus. Due of the extremely

high potential in the area and the orthogonality requirement between various states, the wavefunctions close to the nucleus oscillate quickly, necessitating the need for a very large cut-off energy and basis set. Thankfully, research in physics and chemistry demonstrates that only valence electrons significantly engage in atomic interactions, with core electrons on distinct atoms being independent of their surroundings. As a result, it is possible to assume that the core electron states are stable and to create a pseudopotential for each atomic species that accounts for the interactions between the nucleus and core electrons.

The two forms of pseudopotentials are distinguished by:

i . Norm-conserving Pseudopotential

ii. Ultra-soft Pseudopotential

The calculated and applied norm-conserving pseudopotentials in DFT allow for accurate and efficient ab initio electronic structure computations of intricate polyatomic systems. The following properties are occupied by these pseudopotentials:

- The core atomic states are assumed to be frozen because the majority of the valence electrons determine the majority of the atomic states' physical and chemical characteristics. The term "frozen-core approximation" refers to this.
- The pseudopotential is considerably smoother within the core regions around the nuclei, but beyond the core radius, it must correspond to the true all-electron potential properly. Stated otherwise, the pseudopotential works on smooth pseudo wave functions outside the core area that are comparable to the genuine valence wave functions. However, by ignoring radial nodes, it destroys the orthogonality of the true valence and core orbitals. Consequently, it reduces the computing load by enabling the pseudo wave functions to be extended in terms of whole orthonormal sets, such as plane waves. This is particularly crucial for the numerical solution of the complex systems' Schrödinger and Poisson equations.
- The norm-conservation constraint, which states that these pseudopotentials must operate outside of the core region in the same way as their all-electron counterparts, limits them. Provided that an appropriate potential design is taken care of, non-conservation makes the computations

trustworthy. This is particularly true when it comes to explaining chemical bonds. The ones that need a few fundamental functions to increase electron densities and wave functions are referred to as "soft-potentials." This lessens the effort required for calculation.

3.5 Ab-initio Methods

One type of theoretical approach makes use of the atoms' atomic number and the values of basic constants to compute molecular structures and other crystal characteristics without the need for empirical data is called the ab-initio method. The phrase "ab-initio", obtained from Latin, is formed from the words "ab" (from) and "initio," derived from initium (beginning). When doing ab-initio calculations, several numerical operations are needed, and with the increase in size of the molecule or atom, the processing time grows quickly. The ability to accurately compute the characteristics of both tiny and big molecules has been made possible by advances in computing power, and this type of technique may now replace the semi-empirical method. For a range of molecular geometries, the total energy of the molecule may be determined through the ab-initio calculations, and the conformation with the lowest energy are used to determine the bond angles and lengths of the molecules. Ab-initio approaches are able to converge to the precise solution when approximations are small enough in magnitude. However, there is no monotonic convergence, and for some attributes, the most minute calculation may yield the best result. The ab-initio approach is used to calculate the chemical and physical characteristics of any periodic system with a particular crystalline structure and chemical composition as accurately as possible, without requiring a priori knowledge [45].

The ab-initio techniques that are most popular are:

i. The Hartree-Fock method

ii. The Density Functional Theory (DFT) method.

3.5.1 Hartree-Fock method

A variational method called the Hartree-Fock method yields the wave function of a many-body quantum system, which for fermions is often expressed as a Slater determinant. An approximation approach for determining the ground-state energy and wave function of a quantum many-body system is the Hartree-Fock (HF) method. Many quantum chemistry issues are addressed using this approach, which was first suggested by Hartree in 1928 [51] and then improved by Fock and Slater in 1930 by integrating the Pauli principle. However, the method is often applied in the matrix formulation provided in 1951, by Roothaan [52]. The method is broken down into multiple steps. Initially the HF equations are made up using the Slater determinant for an electronic configuration. The Fock operator is defined, along with the secular equation; it is iteratively solved until self-consistency is achieved. This makes it possible to find a ground-state energy minimum.

The Schrödinger equation of molecules, atoms and solids is often solved using the Hartree-Fock technique, although nuclear physics has made extensive use of it. This article's remaining sections will be devoted to electronic structure theory applications. The HF technique makes the assumption that a single Slater determinant (if fermion particles) or a single permanent (if boson particles) of N spin-orbitals may approximate the system's precise, N-body wave function. A set of N-coupled equations for the N-spin orbitals can be obtained by applying the variational principle. These equations may be solved to obtain the approximate values of the system's energy and HF wave function. The exchange energy is precisely calculated using the HF approach, however the effect of electron correlation is not calculated. It is exceedingly challenging to compute the correlation energy. This is due to the fact that the correlation energy has a direct relationship with the Hilbert space's degrees of freedom, which the single determinant is unable to cover. The vast majority of the wave function approaches include the vacant HF one-electron orbitals in this expansion and include several Slater determinants in an attempt to travel across the Hilbert space. Providing a precise representation of the entire electrical wave function would be the main objective. A 3N-dimensional function of complex nature with N spin coordinates makes up the wavefunction in the

Born-Oppenheimer approximation, where N being the amount of electrons. For small systems, the computing cost of the multi-faceted research for such a wavefunction is practically unsustainable. This being the reason for the DFT analysis, the self-consistent field technique is another name for the Hartree-Fock approach.

The generated non-linear equations' solutions act as though every particle was rendered to the mean-field that every other particle has formed. An iterative fixed-point type approach is used to solve the equations, where this solution strategy is not the only one that may be used, nor is it a necessary component of the HF approach. The electronic characteristics that depend on the crystal's electronic structure are of interest to us. It depends on the electric charge and the geometry of the nuclei, which are assumed to be fixed and organized in a crystalline lattice. Selecting a Hamiltonian is the first crucial step in any ab-initio investigation of electrical structure. Typically, a crystal is made up of 1023 atoms organized in an orderly pattern. Calculating the wavefunction requires consideration of each nucleus and each electron. This wavefunction represents the all-inclusive many body wavefunction that fully characterizes the system.

For this wavefunction, the time-independent Schrödinger equation will look like this.

$H\Psi = E\Psi$

$$\left[-\frac{\hbar^2}{2m}\sum_{i=1}^{N_{el}}\nabla_i^2 - \frac{\hbar^2}{2}\sum_{i=1}^{N_{at}}\frac{\nabla_i^2}{M_i} - \frac{e^2}{4\pi\epsilon_0}\frac{1}{2}\sum_{i,j=1}^{N_{el}N_{at}}\frac{Z_j}{|r_i - R_j|} + \right. \qquad \ldots(23)$$

$$\left. \frac{e^2}{4\pi\epsilon_0}\frac{1}{2}\sum_{i,j=1}^{N_{at}N_{at}}\frac{Z_i Z_j}{|R_i - R_j|} + \frac{e^2}{4\pi\epsilon_0}\frac{1}{2}\sum_{i,j=1}^{N_{el}N_{el}}\frac{1}{|r_i - r_j|} \right] \Psi(r_1 s_1, \ldots r_{N_{el}} s_{N_{el}}; R_1,$$

$$= E\Psi(r_1 s_1, \ldots r_{N_{el}} s_{N_{el}}; R_1, \ldots R_{N_{at}})$$

where the atomic number is denoted by Z, M being the atomic mass, and m is the electronic mass; R is the radius vector for the atom and r is the radius vector for the electron. The all-inclusive many-body wave function Ψ, with energy E has atoms (N_{at}) and electrons (N_{el}), the kinetic expression of the electrons and

nuclei are the left-hand side's first two terms; the electron-nucleus exchange is the third term, the nucleus-nucleus component is the fourth, and the electron-electron transfer is the fifth.

This problem continues to get extensive and complex, thus requiring approximations. The Born-Oppenheimer approximation should be performed first. This implies that the mobility of the nuclei is ignored, and the second part in Eq.(23) can be taken to be equal to zero. Actually, if the lattice constant is kept unchanged, the nucleus-nucleus component will stay unchanged and be equal to zero. In the second, the many-body wavefunction is transformed into a collection of decoupled wavefunctions by using the Pauli principle. This may be accomplished by expressing the entire wavefunction as a Slater determinant of one-electron wavefunctions. An approximation to the entire wavefunction is what a Slater determinant is. The ansatz will appear as

$$\Psi(r_1 s_1, \dots r_N s_N) = \frac{1}{\sqrt{N!}} \begin{vmatrix} \Psi_1(r_1 s_1) & \Psi_1(r_2 s_2) & \cdots & \Psi_1(r_N s_N) \\ \vdots & \vdots & & \vdots \\ \Psi_N(r_1 s_1) & \Psi_N(r_2 s_2) & \cdots & \Psi_N(r_N s_N) \end{vmatrix} \quad \dots(24)$$

where the initial electron wave function at position r_1 with spin s_1 is represented by $\Psi_1(r_1 s_1)$. The electron-electron component is separated into two parts using this ansatz, and the resulting set of one-electron equations is known as the Hartree-Fock equations:

$$\frac{\hbar^2}{2m}\nabla_{\mathrm{i}}^2\psi_i(r,s) - \frac{e^2}{4\pi\epsilon_0}\left(\frac{1}{2}\right)\sum_{\mathrm{j}=1}^{N_{at}}\frac{Z_j}{|\mathrm{r}-\mathrm{Rj}|}\psi_i(r,s) \quad \dots(25)$$

$$+\sum_{\mathrm{j}=1}^{N_{el}}\frac{e^2}{4\pi\epsilon_0}\int \rho(\mathrm{r}')\left(\frac{1}{|\mathrm{r}-\mathrm{r}'|}\right)\mathrm{dr}'\psi_i(r,s)$$

$$-\sum_{\mathrm{j}=1}^{N_{el}}\frac{1}{4\pi\epsilon_0}\int \frac{e^2}{|\mathrm{r}-\mathrm{r}'|}\psi_j^*(r',s_j)\psi_i(r',s_i)\psi_j(r,s_j)\delta_{s_i s_j}dr'$$

$$= \varepsilon_i\psi_i(r,s)$$

where the Kronecker delta is represented by $\delta_{s_i s_j}$ and the electron density by $\rho(r')$. The electron-electron interaction term, which is divided into the direct term and the exchange term, is the final two terms on the

left side of this equation. The Coulomb fields of every other electron are combined in the direct term to form an average field that the electron travels through. The Slater determinant ansatz also satisfies the Pauli principle, which states that the exchange term appears as a result of the anti-summarization of the entire wavefunction. A trial wavefunction for the potential is necessary before the energy can be computed since HF theory implies that an electron moves in a potential that is the average of the potentials owing to all other electrons and nuclei. The Schrödinger equation is then solved repeatedly in order to determine the ideal wavefunction. It implies that a new wavefunction is computed by estimating the wavefunction in the potential terms. The process is then repeated until there is no difference between the old and new wave functions. First, the new wavefunction is used to compute new potential terms. Once this is completed, the Schrödinger equation has an approximate, self-consistent solution. In condensed matter physics, the characteristics of each system are determined by its ground state electronic structure (GSES). Therefore, the primary goals of our attention are the computation of ground state energy and certain other aspects related to energy. As one Slater determinant is insufficient to extend the complete Hilbert space of a set of fully interacting fermions, the Hartree-Fock energy is not the proper ground state energy.

Chemists define the so-called correlation energy as the difference between the total ground state energy and the Hartree-Fock energy:

$$E_c^{che} = E_{total} - E_{HF} \qquad \ldots(26)$$

The exchange energy is precisely calculated using the Hartree-Fock technique, but the influence of electron correlation is not calculated at all. Calculating the correlation energy is an extremely challenging task. This is due to the fact that the correlation energy has a direct relationship with the Hilbert space's degrees of freedom, which the single determinant is unable to cover. By adding numerous Slater determinants and including the unoccupied Hartree-Fock one-electron orbitals in this expansion, most wavefunction approaches attempt to bridge the Hilbert space. To provide an accurate depiction of the entire electrical wavefunction is the aim of this. Here N is the number of electrons, and the Born-Oppenheimer approximation is a wavefunction in the 3N dimensional complex function with N spin coordinates. For

even relatively tiny systems, the computing cost for the pursuit of a multi-dimensional wavefunction is unsustainable. This is the goal of studying density functional theory.

3.5.2 Density Functional Theory

Hohenberg and Kohn [53] devised the DFT. When it comes to explaining the ground state characteristics of insulators, semiconductors, and metals, DFT is a very effective theory as shown by Kohn and Sham [54]. The fundamental idea behind the DFT is to use density rather than the many-body wave function to explain an interacting system of electrons. An alternative to the ab-initio procedure is the DFT. The electronic structure of many-body systems, including molecules, atoms, and condensed phases, as well as electron density that are spatially dependent, are described using this technique, which is based on quantum mechanics. The main objective of DFT is to characterize a dynamic system of fermions using density rather than the many-body wave function [44]. N electrons in a solid follow the Pauli principle, which causes them to separate from one another via the Coulomb potential. This suggests that rather than depending on all 3N degrees of freedom, the system's fundamental variable is dependent on three spatial coordinates: x, y, and z. The computational method that Kohn and Sham (KS) presented in the years that followed serves as the basis for DFT [54], as well as two theorems established in 1964, by Hohenberg and Kohn [53].

They showed the electron density ($\boldsymbol{r}$), that is the important quantity in DFT, is a function of the total energy, suggesting that is all that is needed to understand instead of the complex many-electron wave function [44].

- Theorem 1 (Uniqueness) states that each observable's ground state expectation value is a distinct and unique function of the electron density ($\boldsymbol{r}$) ground-state.

This implies that all of the system's characteristics may be calculated in the ground state provided the electron density and corresponding functions are observed. It is feasible to compute the ground state energy $E_0[\rho_0]$ in particular.

- Theorem 2 (Principle of Variation): The sum of the energy functional [ρ] is decreased by electron density ($\boldsymbol{r}$).

Therefore, for the particular external potential provided by a collection of nuclear charge, the second theorem offers a variational condition for calculating $\rho_0(r)$ and $E_0[\rho]$ jointly.

E.g.

$$V(r) = -\sum_{i,j=1}^{N_{el}N_{at}} \frac{Z_j}{|r_j - R_j|} \quad \ldots(27)$$

The ground state, E_0 is found by minimizing the expression of the form:

$$E[\rho(r)] = \int \rho(r) V(r) dr + \frac{1}{2}\int \frac{[\rho(r)\rho(r')}{|r-r'|} dr dr' + \quad \ldots(28)$$

$$\int \rho(r) g(r;[\rho]) dr + \sum_{i,j=1}^{N_{el}N_{at}} \frac{Z_i Z_j}{|R_i - R_j|}$$

$$= E_{ext} + E_j + E_{kxc} + E_{RepNuc}$$

where $\rho(\boldsymbol{r})$ is the representation of an n-electron density. In equation (28) the charge density ($\boldsymbol{r}$) classical-self-interaction is given by the second component, which reflects the relationship of internal energy with the external potential. The third component included the ($\boldsymbol{r}$) function, and the last term is the typical inter-nuclear repulsion. It may be represented as the correlation energy per unit density at ($\boldsymbol{r}$) and the density of kinetic exchange. It is discovered that 0r corresponds to the lowest value. It is shown that ($\boldsymbol{r}$) is a universal coefficient of the density ρ, however it is unclear how to analyze it. As a result, numerous approximations are used, including the Local Density Approximation (LDA) and the Generalized Gradient Approximation (GGA). The following subsections offer a succinct description of LDA and GGA.

Emphasizing on establishing the system's ground state energy, the Kohn and Sham (KS) technique [45] is computed using the self-consistent field (SCF) process in the following way:

1. For a one-electron effective Hamiltonian, the corresponding eigen-functions (orbitals) and n/2 lowest eigenvalues are determined:

$$\hat{\mathrm{h}}_{eff}\psi_i(r) \equiv \left[-\frac{1}{2}\nabla^2 + V_{eff}(r)\right]\psi_{\mathrm{i}}(r) = \varepsilon_{\mathrm{i}}\psi_i(r) \quad \ldots(29)$$

2. The calculation of density, (***r***):

$$\rho(\mathrm{r}) = 2\Sigma_{\mathrm{i}}|\psi_i(r)|^2 \quad \ldots(30)$$

3. The V_{eff} as a function of the density, (***r***) is recalculated as:

$$V_{eff}(r) = V(r) + \int \frac{\rho(\mathrm{r}')}{|\mathrm{r} - \mathrm{r}'|}dr' + \mu_{xc}(r;[\rho]) \quad \ldots(31)$$

where, $\mu_{xc}(r;[\rho])$ is the exchange-correlation potential.

4. Proceed to step 1 if self-consistency is not attained.

5. Equation (32) is used to derive the ground state energy and $(r) = \rho_0(r)$ (GS density) at self-consistency,

$$E_0 = E_{kps} + \int \rho_0(r)V(r)dr + \frac{1}{2}\int \frac{\rho_0(r)\rho_0(r')}{|r - r'|}drdr' + E_{xc} + E_{RepNuc} \quad \ldots(32)$$

Defining the pseudo-kinetic energy, E_{kps} by,

$$E_{kps} = \Sigma_{\mathrm{i}}\int \psi_{\mathrm{i}}(r)^* \left(-\frac{1}{2}\nabla^2\right)\psi_i(r)dr \quad \ldots(33)$$

The exchange-correlation energy, Exc is expressed as,

$$E_{xc} = \int \rho_0(r)\varepsilon_{xc}(r;[\rho])dr \quad \ldots(34)$$

The application of DFT has shown to be a useful technique for studying crystals' electrical structures. The analytical intricacy of the association and exchange energy formulas requires numerical integrations for its implementation. Using the analytic functions of the electron density and its derivatives, the integrals exhibit an irregular spatial distribution, with sharp edges matching the sites of the nuclei. To accurately calculate the energy transfer of the electron-electron interaction, the following integration has to be used:

$$E^{DFT} = \int_{UNITCELL} \varepsilon^{DFT}(r)dr \quad \ldots(35)$$

where the exchange-correlation interaction, ε^{DFT} is represented by the DFT energy density (DFT). Equation (35) may be used to calculate the ground state energy (GS energy) of an electron and ion system based on its electron density.

3.5.2.1 Local Density Approximation

The simplest and most effective type of approximation is the local density functional approximation, which is simply a general integral across a function of the density at any given location in space. Since the approximation starts with a uniform electron gas, it can only be accurate in the particular case of a uniform electronic system, that is, a system in which the electrons have an infinitely large positive potential selected to maintain the total charge neutrality. Another type of approximation, called local-density approximations (LDA) to the exchange-correlation energy functional in DFT rely only on the electronic density value at all point in space. However, the homogeneity of electron gas (HEG) model has produced the majority of good local approximations. When applied to molecules and solids, functional based on the HEG approximation is commonly used interchangeably with LDA. This equation for exchange-correlation energy is provided by KS [54].

According to the LDA, the exchange correlation energy at a location in a material where the charge density is slowly changing may be thought of as being the same as that of localized uniform electron gas with uniform charge density. In this scenario, we can express E_{xc} as

$$E_{xc}^{LSDA}[\rho] = \int \rho(r)\varepsilon_{xc}[\rho(r)]dr \qquad \ldots(36)$$

This equation for exchange-correlation energy is provided by KS [54]. Additionally, they established the local spin density approximation (LSDA), in which the exchange correlation energy is a function of the local electron-spin densities, $\rho\uparrow$ and $\downarrow$, and spin polarization is permitted.

$$E_{xc}^{LSDA}[\rho\uparrow, \rho\downarrow] = \int \rho(r)\varepsilon_{xc}[\rho\uparrow(r), \rho\downarrow(r)]dr \quad \ldots(37)$$

The total energy E_{tot} in this expression and the single-electron KS equations can be obtained in the following way by using the variational principle:

$$\left\{-\frac{1}{2}\nabla^2 + V_{ext}(r) + V_c[\rho(r)] + \mu_{xc}[\rho(r)]\right\}\psi_i(r) = \varepsilon_i\psi(\mathrm{r}) \quad \ldots(38)$$

Where $\mu_{xc}[\rho(r)] = \frac{\partial E_{xc}[\rho]}{\partial \rho(r)}$

Decomposing the exchange-correlation energy to exchange and correlate terms linearly,

$$E_{xc} = E_x + E_c \quad \ldots(39)$$

so that distinct expressions for E_x and E_c are obtained. The exchange term takes on a simple analytic form for the HEG.

LDA is independent of the gradient of the electron density and solely depends on the value of electron density. The majority of contemporary DFT codes are based on this approximation. In systems with rapidly fluctuating charge density, it even functions fairly well. But it frequently overestimates binding energies and underestimate ionization and ground state energies of atoms. It is known to prefer state configurations with high spin. Due to these factors, efforts have been made to go beyond the LDA, most notably by incorporating longer range gradient effects by adding gradient corrections [55]. But in reality, even if these enhancements appear to produce greater total energies, their resulting structure is frequently inferior and comes at a far higher computational cost. Generally speaking, the LDA gets better with system size and gets worse for tiny molecules. The exchange-correlation energy,E_{xc}, is the sole term in the KS equation's effective potential that cannot be precisely defined.

3.5.2.2 Generalized Gradient Approximation

In general, GGA has a higher probability for producing equilibrium lattice parameters than LDA, and this has a major impact on the ground state properties (solids, molecules and light atoms). When the exchange functional GGA is combined with accurate correlation functional expressions, DFT can be used in a variety of ways to provide structures, bond energies, and reaction activation energies that closely match both the experiment and the most precise ab-initio calculations. More sophisticated approximations are currently used by many DFT-based modern programs to increase accuracy for specific physical attributes. The GGA was utilized in this study's DFT computations. Compared to LDA, the GGA is highly efficient. As previously mentioned, the LDA does not take into account the homogeneity of the actual charge density; instead, it employs the exchange-correlation energy for the uniform electron gas at every point in the system. The exchange-correlation energy can differ greatly from the uniform value for non-uniform charge densities. The gradient and higher spatial derivatives of the total charge density can be used to express this variation. Accounting for this variation, the GGA exploits the charge density gradient.

When the charge density fluctuates gradually in a system, the GGA has shown to outperform the LDA. It can also be applied to the inhomogeneous electron gas system.

A spin-density function, the exchange-correlation energy E_{xc} and their gradients, produces relevant conclusions [45]:

$$E_{xc}^{GGA}[\rho\uparrow,\rho\downarrow] = \int [\rho\uparrow(\mathrm{r}),\rho\downarrow(\mathrm{r}),\nabla\rho\uparrow(\mathrm{r}),\nabla\rho\downarrow(\mathrm{r})]\mathrm{dr} \qquad \ldots(40)$$

The goal of using GGA is to greatly raise the caliber of LDA findings. When there are fast density variations, as there are in molecules, LDA fails. This issue can be solved by taking into account the gradient of the electron density, also known as the GGA.

3.6 CASTEP Computer Code

The computer program CASTEP uses plane wave basis sets and DFT to carry out the first principles calculations and determine the various material properties. Professor M.C. Payne was the creator of CASTEP, and it was further enhanced by some UK research groups [40]. The Cambridge Cavendish Laboratory's Theory of Condensed Matter (TCM) group introduced CASTEP in the late 1980s and early 1990s. CASTEP was primarily an academic application written in Fortran-77 that ran serially. The research community rewrote the code between 1999 and 2001 using Fortran-95 and MPI to take advantage of the features of the contemporary Fortran and to increase software sustainability on parallel machines. Introduction of the improved code design has caused the contemporary techniques and technologies to be quickly incorporated to the CASTEP code. The following is a concise overview of the electronic structure computation process used in CASTEP: The plane-wave pseudopotential method solves the set of one-electron Schrödinger equations [56]. The wave-functions are extended within a plane wave basis set that is defined by the utilization of periodic boundary conditions and Bloch's Theorem.

The primary features of the contemporary plane-wave code are:

i. Parallel design

ii. Advanced

iii. Portability

iv. Clearly defined modular framework

v. Possess the same or superior features configured from the original F77 code.

With its many capabilities, CASTEP, an advanced software designed for the study of basic principles. The code's goal is to ascertain the system's physical attributes using ab-initio calculations; its fundamental calculation is the total energy, from which several other values are obtained. For instance, forces are obtained from the derivative of total energy with respect to atomic locations, while stresses are obtained from the derivative with respect to cell characteristics. Following that, comprehensive geometric

optimizations and finite temperature molecular dynamics are carried out; restrictions and symmetry (both inside and outside the cell) can be applied to the computations automatically using built-in symmetry recognition or as specified by the user. One can use the CASTEP code in parallel or serial fashion. Running in parallel is simple to understand, because CASTEP uses the freeform file format, some commands are required in order to receive the results of a given computation.

The following is a detailed discussion of the CASTEP code's summary:

- Total energies: the sum of the forces, stresses, and energy.
- Electronic structure: electron orbitals, charge densities, band structure, total and partial electronic density of state and the optical characteristics (refractive index, absorption, reflectivity, and dielectric function) in relation to the standard DFT band gap calculations.
- Geometry optimization: optimization of atomic locations and unit cell characteristics under external pressure and stress, either limited or unconstrained.
- Phase transitions: to acquire the phase transitions.
- Exchange and correlation: the LDA and GGA functional are linked to functions like PW91 and PBE functional, although non-local functional such HF exact/screened exchange and weighted density approximation are also accessible.
- Molecular dynamics: Constant temperature, pressure, volume, and energy are a few of the conditions that can be met when doing finite temperature molecular dynamics.

Chapter 4 Results and Discussion

4.1 Structural Properties of $Cs_2LiGaBr_6$

$Cs_2LiGaBr_6$ is a double perovskite $A_2^{1+}M^{2+}M^{3+}X_6^{1-}$ where A_2^{1+} = Cs, M^{2+} = Li, M^{3+} = Ga and X_6^{1-} = Br. $Cs_2LiGaBr_6$ is a cubic, perovskite-derived structure that crystallizes in the $Fm\bar{3}m$ (no. 225) space group. The cubic crystal structure of $Cs_2LiGaBr_6$ geometrically optimized is shown in **Figure 1**. The unit cell of the material contains 40 atoms, distributed as follows: 8 Cs, 4 Li, 4 Ga, and 24 Br atoms.

In the unit cell, distinct atomic positions are defined: Cs atoms occupy a face-centered position at the 8c Wyckoff site, designated by fractional coordinates (0.25, 0.25, 0.25); Ga atoms are positioned at the body-centered site, residing in the 4b Wyckoff site with fractional coordinates (0.5, 0, 0); Li atoms are situated at the corner positions, located in the 4a Wyckoff site with fractional coordinates (0, 0, 0); Br atoms occupy face-centered positions within the 24e Wyckoff site, positioned at fractional coordinates (0.2513, 0, 0). **Figure 1**, illustrates the $Cs_2LiGaBr_6$ unit cell, where Cs^{1+} forms bonds with twelve equivalent Br^{1-} atoms, creating $CsBr_{12}$ cuboctahedra. The cuboctahedra share corners, face, and edges with equivalent $CsBr_{12}$ cuboctahedra, $LiBr_6$ octahedra, and $GaBr_6$ octahedra.

The computed values of the lattice constant, the corresponding unit cell volume and density in this simulation with available experimental results of the cubic $Cs_2LiGaBr_6$ are listed on **Table 1** [32].
The calculated lattice parameters in this study exhibit good consistency with previous theoretical works [32]. With respect to increasing pressure than the experimental findings, the computed lattice constant value is lower.

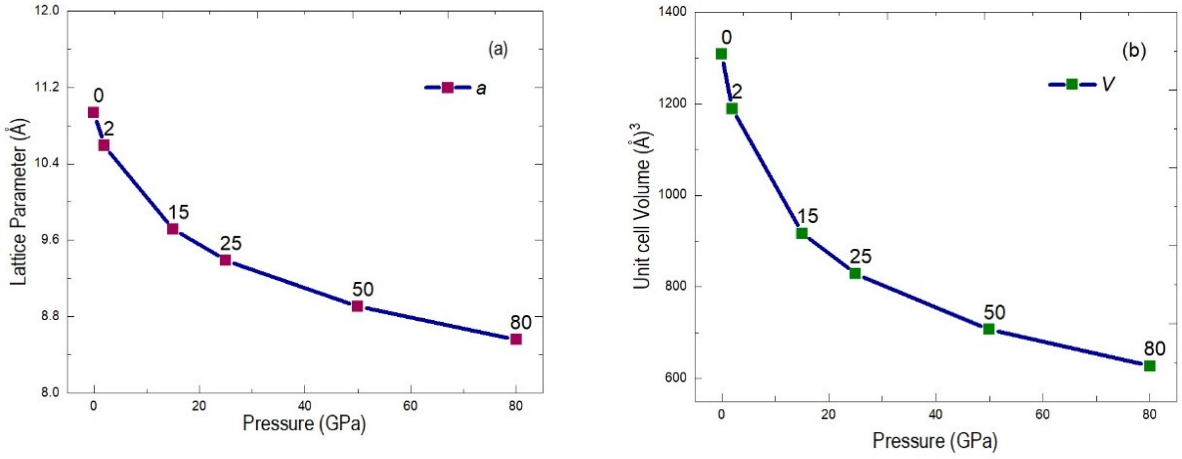

Figure 2: Variation of lattice constant (a) and unit cell volume (V) of cubic $Cs_2LiGaBr_6$ perovskite with pressure.

Table 1: Calculated lattice parameters, unit cell volume and density of $Cs_2LiGaBr_6$.

Compositions, Pressure [GPa]	**Optimized lattice parameter, a [Å]**	**Volume [Å]³**	**Density, ρ [g /cm³]**	**Band-gap**
$Cs_2NaGaBr_6$ [1]	10.96	2221.04	-	-
$Cs_2LiGaBr_6$ [1]	10.7867	2117.34	-	-
$Cs_2LiGaBr_6$, 0 GPa	10.937137	1308.311023	4.172745	1.197
$Cs_2LiGaBr_6$, 2 GPa	10.59583	1189.610379	4.589106	1.206
$Cs_2LiGaBr_6$, 15 GPa	9.715444	917.039554	5.953122	1.424
$Cs_2LiGaBr_6$, 25 GPa	9.391435	828.315754	6.590781	1.564
$Cs_2LiGaBr_6$, 50 GPa	8.909104	707.134603	7.720239	1.793
$Cs_2LiGaBr_6$, 80 GPa	8.559233	627.053448	8.706192	1.854

The unit cell volume corresponding to the density are changing under driving hydrostatic pressure, as shown in **Figure 2.** The values of unit cell volume decreases and density is increased, due to the spatial lattice

positions and the reduced bond lengths. As a result, the repulsive phenomena between atoms have become stronger, increasing the difficulty of crystal compression under applied pressure.

The volume of the compound at 80 GPa decreases and the lattice constant also decreases correspondingly which is expressed by the cell volume formula of the triclinic structure, $V = abcSin\beta$. Correspondingly, as the angle β increases, the cell volume decreases and it is visible that the lattice parameters are the lowest for 80 GPa pressure.

4.2 Optical Properties

A simple and efficient thermodynamic method for improving the efficiency of $Cs_2LiGaBr_6$ as a solar harvesting device and in the application of other optical electronic devices is pressure variation. The optical properties of the materials used to make high-energy solar harvesting material are determined by their electronic configuration. The lead-free, halide double perovskite $Cs_2LiGaBr_6$ performs well in photovoltaic materials due to its high optical conductivity and absorption. In this study, the real and imaginary parts of the dielectric function components of the cubic $Cs_2LiGaBr_6$ perovskite, as well as the absorption coefficient, photoconductivity, and reflectivity, have been studied thoroughly at different hydrostatic pressures of 0, 2, 15, 25, 50, and 80 GPa. At photon energies of up to 30 eV, the following properties have been explored to gain understanding of how the material responds to high-energy radiation.

4.2.1 Optical Absorption

The optical reflectivity and absorption spectra of a substance indicate how well it can absorb light energy. It provides vital information regarding the material's ability to convert UV energy, which is required for the development of ultraviolet devices and in its application in solar cells. An essential component in

comprehending the electronic properties of metallic, semiconducting, and/or insulating materials is the absorption coefficient, or **α**. For electronic transitions (direct or indirect) that take place in the energy bands, the optical absorption coefficient is equally important.

The **Figure 3(a), (b)** shows the **α** of $Cs_2LiGaBr_6$ compound under applied pressure. **Figure 3(a)** is a closeup of the absorption coefficient, from 0-5 eV range photon energy. It shows the absorption edge of the metal halide is shifted in the direction of the low energy region (red shift) with reduced pressure. From the close up of the **Figure 3(a),** we see there is a peak at the visible photon energy range, between 1.63 to 3.26 eV values. The optical absorption of the compound starts to increase with the increasing photon energy at the 7.5eV value and it reaches a maximum at around 10eV for 80 GPa and then reduces gradually.

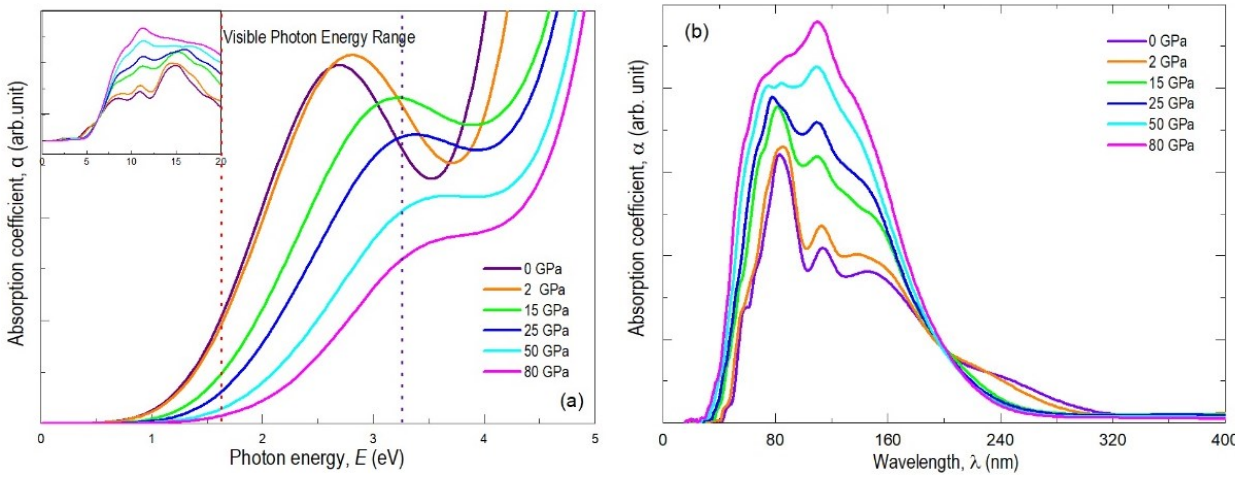

Figure 3: Calculated optical absorption of $Cs_2LiGaBr_6$ as a function of incident photon energies

The **α** is maximum at the Ultraviolet Region (UVR), primarily focusing on the range of UV-C. **Figure 3(b)** shows the **α** of these compositions is maximum in the UVR (100-300 nm) range of the spectrum. The pressure-induced in $Cs_2LiGaBr_6$ enhances the absorption to a remarkable extent in the UVR. Enhancing the absorption of visible light will potentially boost the overall efficiency of solar cells by enabling the conversion of a wider range of light energy into electrical energy [26], [25], [12]. **Figure 3(b)** demonstrates that the absorption coefficient increases steadily beyond 80 nm and peaks at 80 GPa at a distance of

approximately 120 nm. This absorption peak is prominently seen in the Ultraviolet region (UV-C), namely in the 100–250 nm range, and shows great promise for use in UV devices.

4.2.2 Dielectric Function

The static peak of the dielectric function can be used to determine the charge carrier recombination rate. The material's reaction to an external electric field is reflected in the real component of the dielectric function, which influences optical properties like refractive index, light propagation, and phenomena like reflection and transmission [25], [27]. In contrast, energy absorption and dissipation under an electric field are represented by the imaginary component, which is important for applications in photovoltaics and light-emitting devices [25], [27].

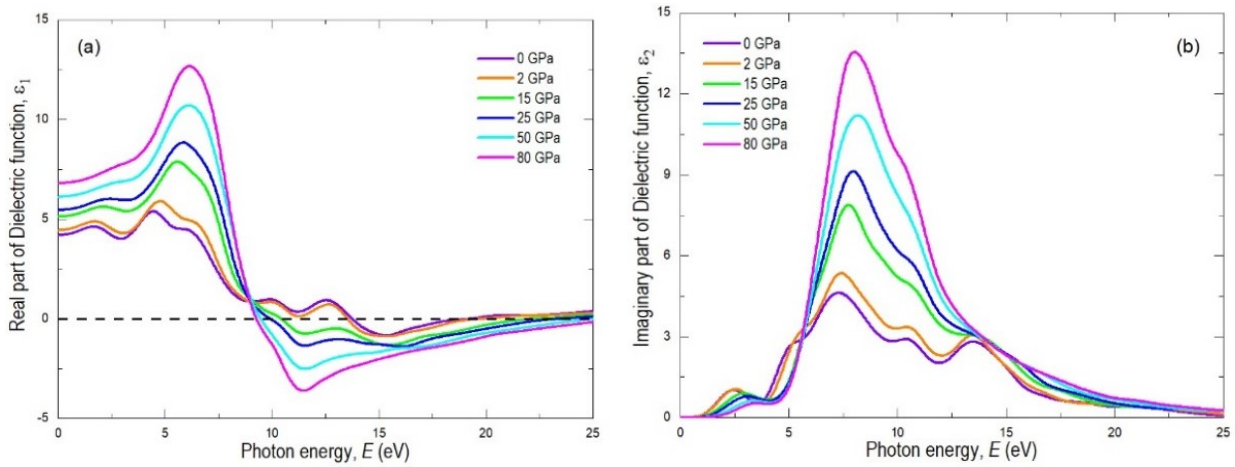

Figure 4: Computed real part (a) and the imaginary part (b) of the dielectric function.

Optical-electronic device performance can be seen from the dielectric function. **Figures 4 (a), (b)** show the real (ϵ_1) and imaginary (ϵ_2) components of the dielectric constant at different pressures. Pressure-induced compounds shown in **Figure 4(a)** have a significant peak at 7 eV and discrete peaks at 2.5 eV, 5 eV, and 7 eV which gradually attenuate as pressure increases. The peak at 7 eV becomes quite distinctive at 80 GPa;

at the UV spectrum. The imaginary part of the dielectric constant is shown in **Figure 4(b)**. Similar to the real part, the imaginary component of the UV spectrum rises with applied pressure; the peaks move towards higher photon energies, mimicking the behavior of optical absorption.

4.2.3 Optical Conductivity

Another kind of optical conductivity is photoconductivity, which is the ability of a material to conduct electricity when exposed to an electromagnetic field. Electrical conductivity and photoconductivity both increase with increased photon absorption. The pressure-dependent optical conductivity (σ_1 real and σ_2 imaginary component) at different pressures is shown in **Figures 5(a), (b).** The real part of optical conductivity determines a material's ability to conduct electricity without losing energy when exposed to light, influencing the material's transparency and conductive qualities. In the meantime, the imaginary part shows how electromagnetic energy is absorbed and dissipated by the substance. This is essential to comprehending its optical absorption properties and optoelectronic device performance [25], [27]. Because of the increasing absorption coefficient with pressure, **Figure 5(a)** illustrates how the optical conductivity increases with rising pressure. Based on the electronic band structure calculations presented in **Figure 5(a),** it is evident that there is no electronic band gap in the compound due to its nonzero photoconductivity at zero photon energy. It starts at 0 eV and reaches its maximum value of σ_1 (real component) at 7.5 eV for 80 GPa. The material exhibits high conductivity at 80 GPa. Additionally, a little peak at 2.5 eV is discernible. When exposed to light, the material shows enhanced conductivity or efficient electron flow at that specific energy level, as indicated by these two peaks in the real component of optical conductivity.

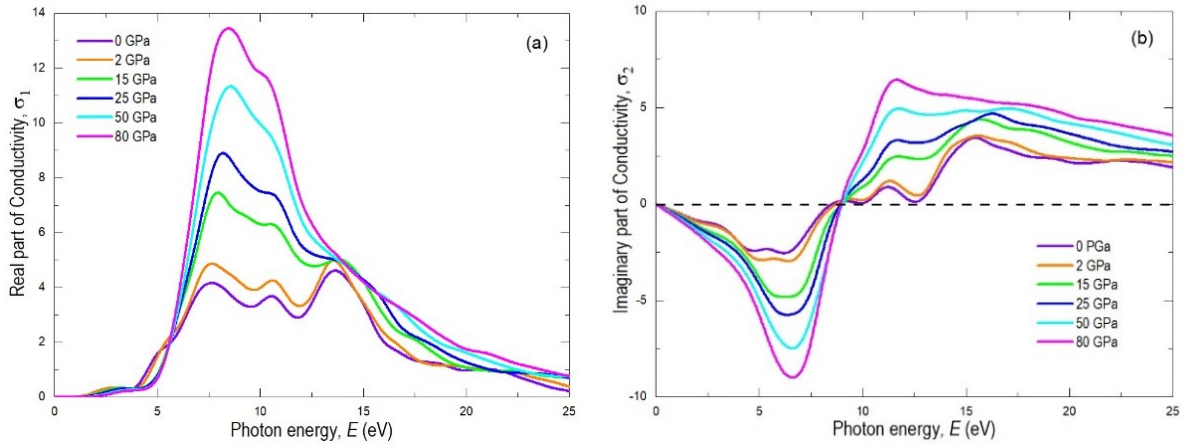

Figure 5: Computed spectra of the real part (a) and the imaginary part (b) of conductivity under varied pressures.

These peaks also imply that the material efficiently absorbs photons with energy between 2.5 and 7.5 eV, which increases electrical conductivity by causing charge carriers like electrons or holes to be produced.

The sample's negative photoconductivity could be attributed to a decrease in the number of charge carriers in the presence of radiation. The optical features' intra-band contribution can be found in the high-energy ultraviolet region of the spectra, shown in **Figure 5(b)**. For all pressures, the photoconductivity peaks in the UVR region (7.5–10 eV). Similar to the trend seen in optical absorption, the values of the imaginary component of conductivity in the UVR increase with applied pressure and the peaks move to an area with high photon energy. The imaginary component of the dielectric function increases from negative to positive as one goes into the higher photon energy regions.

4.2.4 Optical Reflectivity

The capacity of a substance to reflect incident light energy off its surface is measured by its reflectivity, R. **Figure 6** displays the reflectance of $Cs_2LiGaBr_6$ at different applied pressures. For every compound, it is observed that the reflectivity increases gradually starting at 5 eV, reaching its maximum at 10 eV to 12.5

eV photon energy with a pressure of 80 GPa. The greatest reflectivity for the 80 GPa pressure is observed at 10eV to 12.5eV photon energy, and the value of R is growing continuously from 5eV. For materials suitable for solar cells and other optical absorption applications, the low reflectivity is preferable.

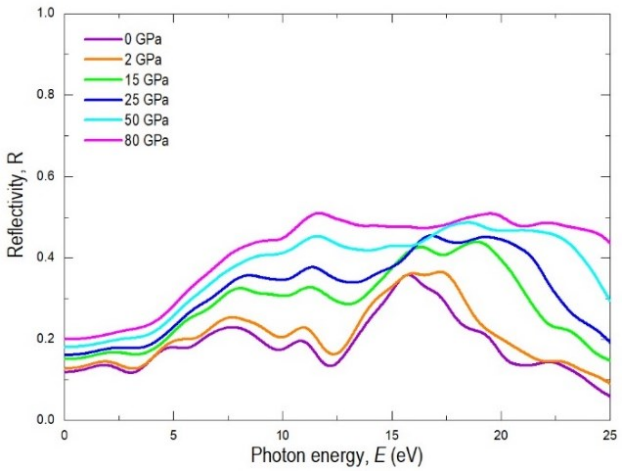

Figure 6: Computed spectra of reflectivity under varied pressure

4.3 Electronic Properties

4.3.1 Band structure

In order to see various electronic and bonding properties, including conductivity, thermoelectric phenomena, and magnetic properties, a strong understanding of the electronic band structure is important. In this study, PBE functional and the GGA approximation have been used for the electronic band structure of the $Cs_2LiGaBr_6$ compound. For $Cs_2LiGaBr_6$ compounds within the first Brillouin zone, the G - F - Q - Z - G energy dispersion ways are examples of high symmetry k-space directions that have an impact on the behavior of these electrons.

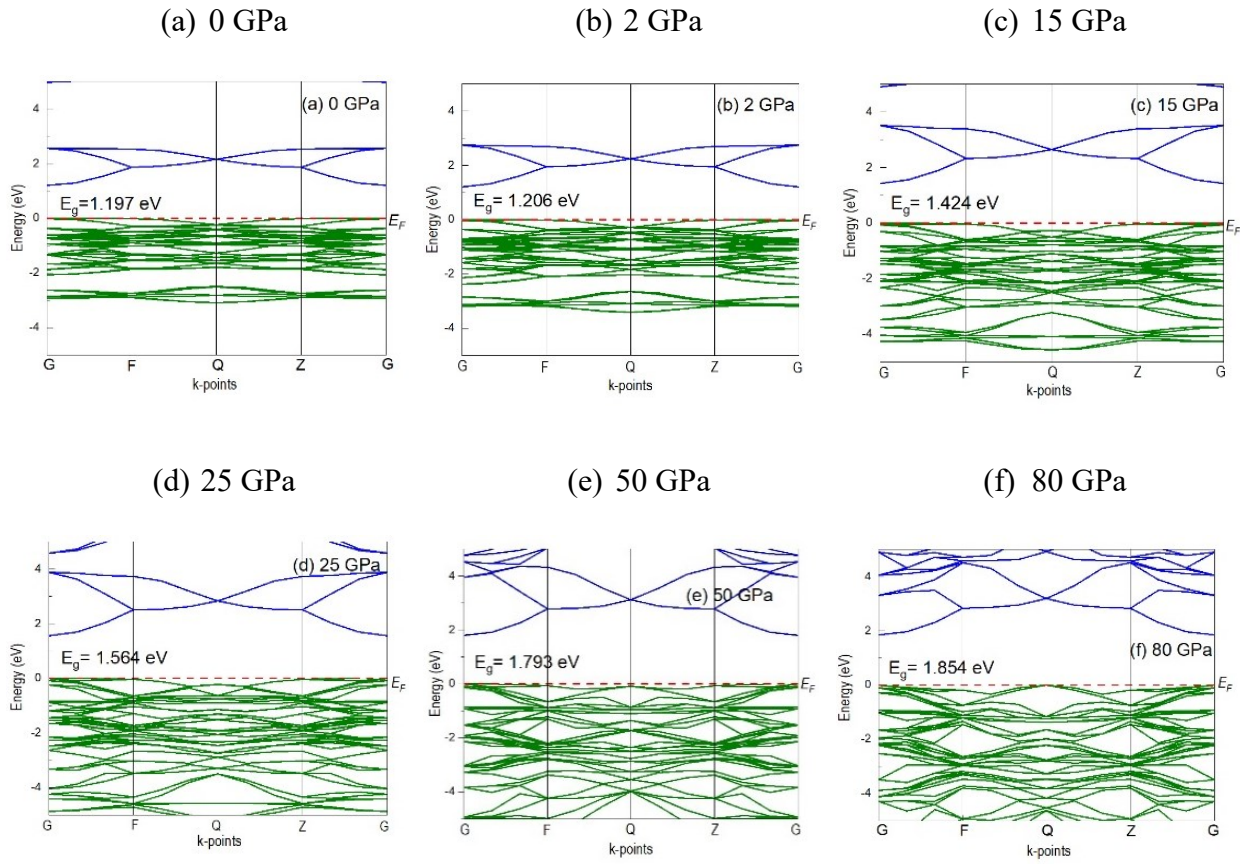

Figure 7: Band structure diagram of $Cs_2LiGaBr_6$ under (a) 0 GPa, (b) 2 GPa, (c) 15 GPa, (d) 25 GPa, (e) 50 GPa and (f) 80 GPa pressure.

For every sample, the *EF* is displayed at the photon energy scale's zero. A crucial criterion for understanding the physical properties of the material is the band structure of the substance near the Fermi level (*EF)* [27], [29]. As a result, the band structure arrangement surrounding the *EF* has been primarily highlighted. In **Figure 7**, the valence band lies between −5 and 0 eV and the conduction band lies between 0 and 5 eV. When a system of fermions is at absolute zero temperature, the energy of the highest occupied quantum state is referred to as the Fermi level. From the band diagram, **Figure 7**, the electronic structures of the compounds are increasing with the increase of hydrostatic pressure. The compound's conduction band minimum (CBM) and valence band maximum (VBM) are found at the G point in the Brillouin zone for pressures of 0, 2, 15, 25, 50, and 80 GPa, respectively. The conduction band minimum (CBM) and valence

band maximum (VBM) align at a common k-point, displaying a direct bandgap across all the structures. **Table 1** indicates that $Cs_2LiGaBr_6$ has a bandgap of 1.197 eV at 0 GPa pressure. Pressure has a substantial influence on the bandgap of $Cs_2LiGaBr_6$ perovskites, and quantum confinement effects are important in the calculated changes. Consequently, when pressure increases, the bandgap likewise does so. It reaches a maximum value of 1.854 eV for applied pressure of 80 GPa, as seen in **Figure 7**, and decreases to 1.206 eV for 2 GPa, 1.424 eV for 15 GPa, 1.564 eV for 25 GPa, and 1.793 eV for 50 GPa.

Compressive strain modifies the quantum confinement when hydrostatic pressure is applied, limiting the mobility of charge carriers inside the crystal lattice [30]. The bandgap energy rises as a result of the improved bonding interactions brought about by that altered confinement. Due to the material's reduced dimensions under pressure, quantum confinement effects limit the migration of charge carriers within nanoscale dimensions, impacting their energy levels and, consequently, the bandgap [30], [46], [32], [31]. Because of this, $Cs_2LiGaBr_6$ perovskites' bandgap varies significantly across the range of applied pressure, demonstrating how quantum confinement and compressive strain interact intricately to modify the material's electrical characteristics. Moreover, hybridization between the Br-4s and Br-4p orbitals may be inhibited at high pressure. The patterns of hybridization between different atomic orbitals can also be altered by high pressure [47]. Where there is an orbital alignment at the same energy level, hybridization occurs. Consequently, a reduction in the contribution of Br-4p orbitals pushes the top edge of the valence band to higher energies and effectively widens the bandgap.

A band gap between 1.0 and 1.7 eV permits the discharge of electrons without producing excessive heat, which makes it a useful semiconductor for solar applications [48], [25]. The investigated compounds have straight band gaps that are within the visible solar energy spectrum's effective range, which makes them excellent choices for solar cell applications. While direct band gaps are present in certain newly studied double perovskites, their levels are outside of the effective solar range.

4.3.2 Density of States

The density of states (DOS), which goes beyond band structures and band gaps, is used to understand how each component contributes to the compounds' CBM and VBM. Both the total and partial DOS for the compound are shown in **Figure 8** and **9**. According to **Figure 9(a)**, the Br atoms are the source of the VBM, with the Br-4p orbital contributing significantly more than the Br-4s and all other orbitals of contributing atoms combined. The combined influence of the atomic orbitals of Ga and Br makes up the CBM. There is also a noteworthy effect of pressure on the $Cs_2LiGaBr_6$ combination. The existence of the Br-4p states is dramatically reduced with increasing pressure on the pristine sample.

The valence band moves near the Fermi level with pressures of 2 GPa, and further pressures cause a large reduction in its total density of states. A lower interatomic distance results from the lattice constant compressing under increased pressure. Increased overlap between atomic orbitals may result from this, especially between the most active outermost orbitals in $Cs_2LiGaBr_6$ (Br-4p and Cs-5p), which are more sensitive to pressure. This is further supported by **Figure 10's** electron charge density map. Higher orbital overlap increases the bonding consequently lowering the energy levels. The flattening of the valence band at the Fermi level is explained by this.

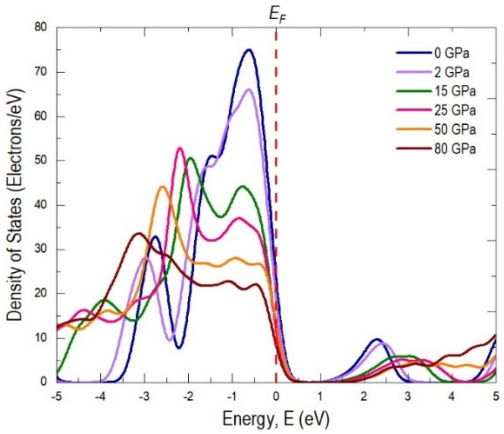

Figure 8: Pressure-dependent TDOS value of $Cs_2LiGaBr_6$ near the Fermi level

It is also possible that at extremely high pressure, the hybridization patterns between various atomic orbitals would alter. This can cause the material's charge density to be redistributed, which could have an impact on the energy levels of particular orbitals like Br-4p. The electron density study in **Figure 10** confirms the observed decrease in the overall density of states at higher pressures, which might potentially be explained by such charge redistribution. It has been observed that under some circumstances, high pressure can cause new electronic states to arise that were not present under ambient settings [49]. These additional states might result from hybridization effects or from changes in the lattice symmetry. They have a considerable impact on the band structure and total density of states.

Figure 10 represents the total electric charge density of $Cs_2LiGaBr_6$ with pressure variation; they were evaluated using the electronic charge density along crystallographic planes oriented along (100). The overall electron density was shown using a color-coded scale, where red (0.00) denotes areas with low charge density and blue (4.00) indicates areas with high charge density.

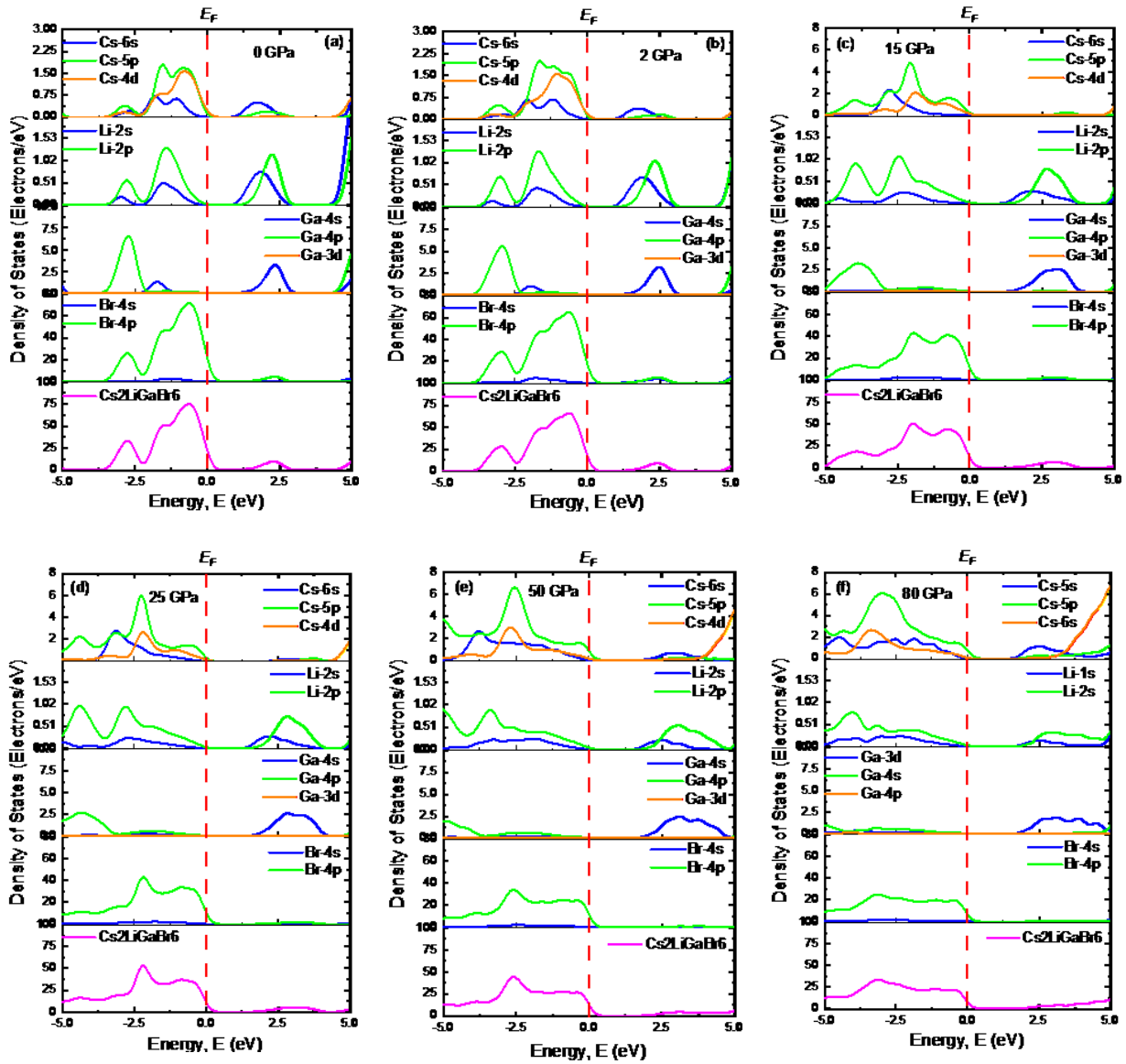

Figure 9: The density of states (DOS) and partial DOS (PDOS) of (a) 0 GPa, (b) 2 GPa, (c) 15 GPa, (d) 25 GPa, (e) 50 GPa and (f) 80 GPa pressure of $Cs_2LiGaBr_6$ compound.

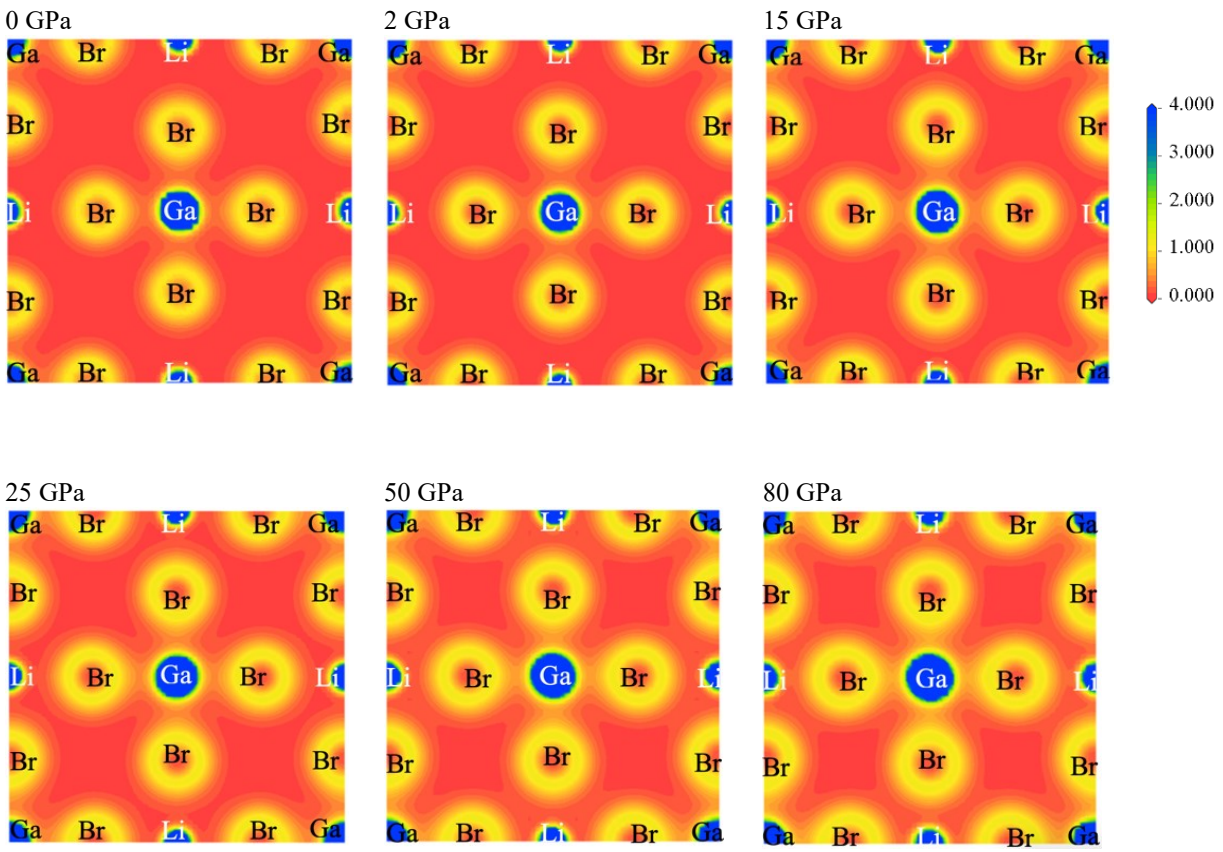

Figure 10: The electronic charge density map for $Cs_2LiGaBr_6$ under pressure of (a) 0 GPa, (b) 2 GPa, (c) 15 GPa, (d) 25 GPa, (e) 50 GPa, and (f) 80 GPa.

Spherically shaped charge densities overlap in the samples under study. Ionic interactions result in electron-rich Ga and electron-poor Br atoms in the 0 GPa pressure sample. The crystal's atoms are forced closer together as pressure rises. As a result, the electron clouds of nearby atoms overlap more because the interatomic distances are shortened. A shift of electron density inside the crystal may also result from increasing overlap and higher pressure. Pressure may drive some electrons in $Cs_2LiGaBr_6$ to move from the Li or Cs cations to the Br anions, reinforcing the bonds and boosting the electron density overall. The bandgap of $Cs_2LiGaBr_6$ perovskites is greatly affected by pressure, as a result of enhanced quantum confinement effects induced by compressive strain. These effects increase bandgap energy and enhance bonding by limiting the mobility of charge carriers inside the crystal lattice [47].

4.4 Mechanical Properties

In order to fully understand the mechanical characteristics of the $Cs_2LiGaBr_6$ metal halide, it is important to look at how pressure affects the elastic constants, as the lattice parameter decreases with applied pressure. The elastic constants are essential parameters for solid materials, which provide a strong connection between the mechanical attributes and valuable insights into the characteristics of forces that are present in solids, with regard to material stiffness and stability [3], [4]. Additionally, elastic constants offer information regarding a crystal's capacity to withstand external pressure. In this study, the elastic constants, namely C_{11}, C_{12}, and C_{44}, of the cubic crystal structure were computed utilizing the CASTEP algorithm and finite strain theory [28], [33]. Whether the elastic constants satisfy the defined Born stability requirements determines whether a cubic crystal is stable [50].This can be stated as follows:

$$C_{11} > 0,\ C_{44} > 0,\ C_{11} + 2C_{12} > 0 \text{ and } C_{11} - C_{12} > 0$$

Table 2 demonstrates that the $Cs_2LiGaBr_6$ metal halide meets the above stability criteria, indicating that it is mechanically stable under significant variation pressure. When the elasticity in length is correlated with the elastic constants, which evolve with higher pressure, the values of C_{11}, C_{12}, and C_{44} increase rapidly as the pressure rises [5]. On the other hand, C_{44} is associated with shape elasticity, which establishes a relationship between shape deformation and stiffness [5]. One widely used parameter to show whether materials are brittle and ductile is the Cauchy pressure (C_{12}-C_{44}).

A material's brittle nature can be determined by looking at its positive Cauchy pressure value. **Table 2** shows that the $Cs_2LiGaBr_6$ perovskite's Cauchy pressure value is positive at zero pressure and grows with pressure increase, indicating that the perovskite's ability to disperse stress and resist crack propagation. The mechanical parameters of the cubic $Cs_2LiGaBr_6$ metal halide present in **Table 3**, include Bulk modulus (B), Shear modulus (G), Young's modulus (E), Pugh's ratio (B/G), Poisson's ratio (v) and Vickers hardness (H_v)

are determined using derived elastic constants; using data collected from CASTEP and the Voigt-Reuss-Hill (VRH) averaging techniques.

Table 2: The values of the Cauchy pressure $\mathbf{C_{12} - C_{44}}$ (GPa) and **Cij** (GPa) of cubic $Cs_2LiGaBr_6$'s perovskite at varying pressures were computed.

	C_{11}	C_{12}	C_{44}	$C_{12} - C_{44}$	$C_{11} - C_{12}$	$C_{11} - 2C_{12}$
0 GPa	21	15.24	14.625	0.62	5.75	51.49
2 GPa	35.86	20.88	17.58	3.29	14.98	77.63
15 GPa	129.05	55.13	39.97	15.15	73.91	239.31
25 GPa	193	81.67	55.1	26.57	111.33	356.34
50 GPa	332	140.53	88.49	52.04	191.47	613.06
80 GPa	489.73	207.27	124.11	83.16	282.45	904.27

At zero pressure, the $Cs_2LiGaBr_6$'s lower values for Bulk, Shear and Young's moduli shows it is a malleable and ductile substance. **Table 3** shows that the increase in pressure increases the values of the B, G and E moduli, suggesting the hardness of the $Cs_2LiGaBr_6$'s is related to the hydrostatic pressure. The pressure induced compositions are promising candidates for optical electronic applications, where lower bulk modulus enables conforming to device shapes in thin-film applications.

Comparing the pressure-induced $Cs_2LiGaBr_6$ to the investigated compounds, a progressive increase in hardness (H_v), Young's modulus (Y), and shear modulus (G) is observed.

Table 3: The generated mechanical properties of $Cs_2LiGaBr_6$ at a different pressure.

	Bulk modulus B (GPa)	**Shear modulus G (GPa)**	**Young's modulus E (GPa)**	**Pugh's ratio (B/G)**	**Poisson's ratio (v)**	**Hardness (H_v)**
0 GPa	15.95	1.916	5.51	8.32	0.442	0.073
2 GPa	25.873	12.45	32.158	2.078	0.292	1.725
15 GPa	79.77	38.74	100.03	2.059	0.291	5.397
25 GPa	118.786	55.32	143.67	2.147	0.298	7.452
50 GPa	204.39	91.35	238.46	2.237	0.305	11.877
80 GPa	301.426	130.644	342	2.307	0.31	16.534

Another key indicator of a crystal's brittle and ductile characteristics is its Pugh's ratio. The brittle nature of the material is indicated by the low value of Pugh's ratio, and the value 1.75 [7] is considered to be the critical value. According to **Table 3**, the Pugh's ratio value of $Cs_2LiGaBr_6$ metal halide at zero pressure is higher than the critical value, indicating that the metal halide is ductile. Additionally, **Table 3** shows that the Pugh's ratio value rises with pressure after experiencing a sharp decline from the initial 0 GPa pressure point. This suggests that increasing pressure can enhance the ductility of $Cs_2LiGaBr_6$.

A valuable criterion for learning about the bonding forces and stability of a crystal is the Poisson's ratio. For ionic crystals, the maximum and lowest values of Poisson's ratio are thought to be 0.5 and 0.25, respectively, for the central forces that are currently present [8]. Interatomic forces are key factors in ionic crystals [8]. **Table 3** shows that, under ambient conditions, the value of Poisson's ratio of the $Cs_2LiGaBr_6$ metal halide is 0.442, which is more than 0.25 but less than 0.5, suggesting the presence of central forces

in the metal halide. The obtained Poisson's values are in close proximity to the value of 0.3, suggesting that central forces predominate among the interatomic forces in $Cs_2LiGaBr_6$. In order to distinguish between a material's brittle and ductile characteristics, a crucial value of Poisson's ratio is 0.26 [6].

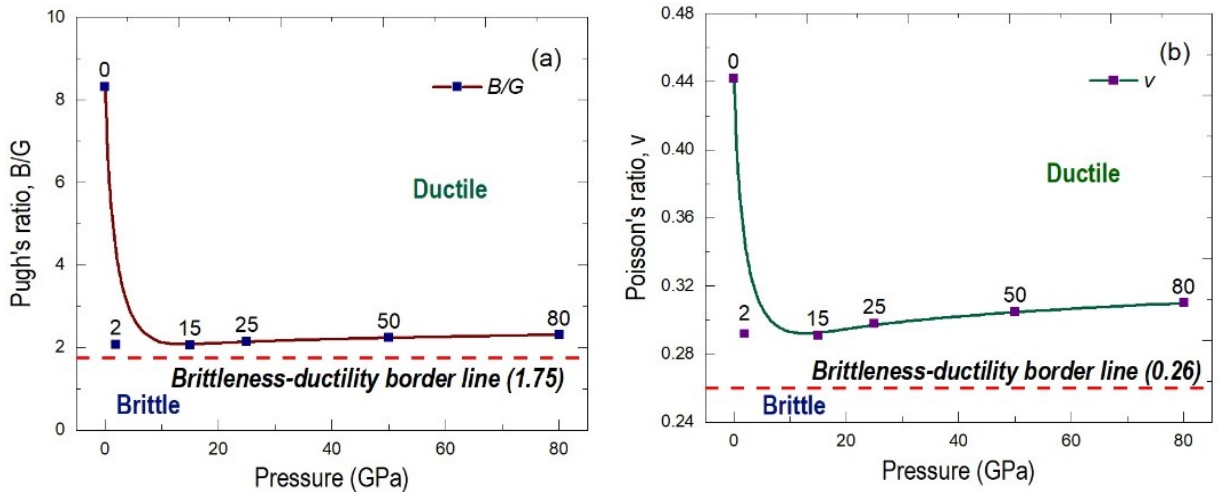

Figure 11: Trend of the (a) Pugh's ratio and (b) Poisson's ratio of $Cs_2LiGaBr_6$ perovskite at a different pressure.

Given that the value of Poisson's ratio rises as pressure increases, adding external pressure is predicted to further improve ductility. Our study reveals $Cs_2LiGaBr_6$ exhibits excellent mechanical properties which could make it a potential candidate for device shapes in thin-film applications.

The values of Poisson's ratio (v) and Pugh's ratio (B/G), the two crucial measures of a material's brittleness and ductility, were found to be within normal thresholds, indicating that all of the pressure-induced compositions are ductile [27], [49]. To provide a clearer understanding of the ductile behavior of the perovskite, **Figure 11** displays the fluctuation of Pugh's ratio and Poisson's ratio of $Cs_2LiGaBr_6$ perovskite with pressure. It is clear from **Figure 11** that $Cs_2LiGaBr_6$ compounds ductility rises gradually with increased pressure; thus, when ductility is needed to construct $Cs_2LiGaBr_6$ devices, pressure can be an effective method.

Chapter 5 Conclusion

The optical, electrical, structural and mechanical characteristics of the $Cs_2LiGaBr_6$ double halide perovskites are studied throughout the investigation by the use of DFT-based first-principles calculations. The analysis of the effects of hydrostatic pressures between 2 and 80 GPa forms the basis of this work.

The optical properties conclude that the absorption coefficient reaches its maximum in the ultraviolet region (UVR), with the greatest intensity in the UV-C range. Under UVR, a further strong absorption peak is seen between 1.63 and 3.26 eV, suggesting that the $Cs_2LiGaBr_6$ perovskite may perform significantly better in solar cells and other optoelectronic device applications. For the highest induced pressure, the real and imaginary components of the dielectric function of $Cs_2LiGaBr_6$ show a strong peak in the UV energy range area. Additionally, the peak is oriented toward higher photon energy. The emergence of a distinct peak in the imaginary portion of the $Cs_2LiGaBr_6$ sample's dielectric function at 7.5 eV (UVR) suggests that the sample has strong UV absorbance, which is consistent with the absorption spectra. A recurring trend, under increased pressure, both the optical absorbance and conductivity greatly increase in the UV areas. There is little reflection at the initial 0 GPa pressure. The reflectivity rises incrementally with the pressure, where the total reflectivity is just marginally higher than 0.5 thus it has poor reflection.

The electrical properties show that the hydrostatic pressure has a considerable impact on the bandgap, which changes from 1.21 eV at 2 GPa to 1.85 eV at 80 GPa. Calculations of the electronic band structure reveal that each compound has a straight bandgap. As the applied pressure increases, the band-gap widens, leading from a semiconducting to metallic transition in $Cs_2LiGaBr_6$ at high pressures. This is because the movement of charge carriers within nanoscale dimensions is limited by quantum confinement phenomena, which cause the material to shrink under pressure. Pressure-induced $Cs_2LiGaBr_6$ exhibited improved optical absorption behavior and photoconductivity in combination with a tunable bandgap. For solar cell applications, straight band gaps are a great option since they fall within the effective region of the visible solar energy spectrum.

The ductile character of pressure-induced $Cs_2LiGaBr_6$ is highlighted by the mechanical stability, which is verified by the elastic constants corresponding with the Born stability requirements and the positive Cauchy pressure values. At pressures of 0 GPa and 80 GPa, the bulk modulus values are 15.95 and 301.4, respectively. Poisson's and Pugh's ratio analysis demonstrates that as applied pressure increases, there is a growing affinity towards ductility. Additional mechanical properties such as bulk modulus, shear modulus, Young's modulus and hardness parameter demonstrate that these materials are stable and suitable for thin-film manufacturing. All things considered, this work represents a significant advancement toward environmentally benign and sustainable options in the rapidly changing field of photovoltaic applications. This highlights $Cs_2LiGaBr_6$ versatile potential in a range of environmental settings.

References

[1] N. R. Wolf, B. A. Connor, A. H. Slavney and H. I. Karunadasa, "Doubling the Stakes: The Promise of Halide Double Perovskites.," *Angewandte Chemie International Edition.,* vol. 60, no. 30, pp. 16264-16278, 2021.

[2] O. D., "Development and the environment in the next two decades.," *Minerals and the Environment.,* vol. 2, no. 2, pp. 69-77., 1980.

[3] J. B. Goodenough, " Energy storage materials: A perspective.," *Energy Storage Materials.,* vol. 1, pp. 158-161, 2015.

[4] E. T. McClure , M. R. Ball, W. Windl and P. M. Woodward, "Cs2AgBiX6 (X = Br, Cl): New Visible Light Absorbing, Lead-Free Halide Perovskite Semiconductors," *Chemistry of Materials.,* vol. 28, no. 5, pp. 1348-1354, 2016.

[5] M. Kulbak, S. Gupta, N. Kedem and e. al., " Cesium Enhances Long-Term Stability of Lead Bromide Perovskite-Based Solar Cells.," *The Journal of Physical Chemistry Letters,* vol. 7, no. 1, pp. 167-172, 2015.

[6] G. F. Heidari and D. Velauthapillai, "A Review on Cs-Based Pb-Free Double Halide Perovskites: From Theoretical and Experimental Studies to Doping and Applications.," *Molecules,* vol. 26, no. 7, p. 2010, 2021.

[7] W. Shockley and H. J. Queisser, "Detailed Balance Limit of Efficiency of p-n Junction Solar Cells.," *Journal of Applied Physics,* vol. 32, no. 3, pp. 510-519, 1961.

[8] A. Datas, E. López, I. Ramiro and e. al., "Intermediate Band Solar Cell with Extreme Broadband Spectrum Quantum Efficiency.," *Physical Review Letters,* vol. 114, no. 15, 2015.

[9] C. Momblona, O. Malinkiewicz, C. Roldán-Carmona and e. al, "Efficient methylammonium lead iodide perovskite solar cells with active layers from 300 to 900 nm.," *APL Materials.,* vol. 2, no. 8, p. 081504, 2014.

[10] K. Wang, Z. Jin, Liang and et al., "All-inorganic cesium lead iodide perovskite solar cells with stabilized efficiency beyond 15%.," *Nature Communications,* vol. 9, no. 1, 2018.

[11] M. Kulbak, S. Gupta, N. Kedem and e. al., "Cesium Enhances Long-Term Stability of Lead Bromide Perovskite-Based Solar Cells.," *The Journal of Physical Chemistry Letters.,* vol. 7, no. 1, pp. 167-172., 2015.

[12] S. Dani, A. Arya, H. Sharma and e. al., "Structural and electronic properties of double perovskite ruthenates; A2GdRuO6 (where A = Ba, Sr).," *Journal of Alloys and Compounds.,* vol. 913, p. 165177, 2022.

[13] A. Kojima, K. Teshima, Y. Shirai and T. Miyasaka, "Organometal Halide Perovskites as Visible-Light Sensitizers for Photovoltaic Cells.," *Journal of the American Chemical Society.,* vol. 131, no. 17, pp. 6050-6051, 2009.

[14] W. Zhang, G. Eperon and H. Snaith, "Metal halide perovskites for energy applications.," *Nature Energy. ,* vol. 1, no. 6, 2016.

[15] W. Yin, T. Shi and Y. Yan, "Unique Properties of Halide Perovskites as Possible Origins of the Superior Solar Cell Performance.," *Advanced Materials.,* vol. 26, no. 27, pp. 4653-4658., 2014.

[16] A. Babayigit, D. Duy Thanh, A. Ethirajan and e. al., "Assessing the toxicity of Pb- and Sn-based perovskite solar cells in model organism Danio rerio.," *Scientific Reports. ,* vol. 6, no. 1, pp. 1-11, 2016.

[17] T. Berhe, W. Su, C. Chen and e. al., "Organometal halide perovskite solar cells: degradation and stability.," *Energy & Environmental Science.,* vol. 9, no. 2, pp. 323-356, 2016.

[18] I. Benmessaoud, A. Mahul-Mellier, E. Horváth and et al., "Health hazards of methylammonium lead iodide based perovskites: cytotoxicity studies," *Toxicology Research. ,* vol. 5, no. 2, pp. 407-419, 2016.

[19] C. Torrence, C. Libby, W. Nie and J. Stein, "Environmental and health risks of perovskite solar modules: case for better test standards and risk mitigation solutions.," *iScience. ,* vol. 0, no. 0, 2022.

[20] H. Min, D. Lee, J. Kim and e. al., "Perovskite solar cells with atomically coherent interlayers on SnO2 electrodes.," *Nature.,* vol. 598, no. 7881, pp. 444-450, 2021.

[21] N. Mardirossian and M. Head-Gordon, "Thirty years of density functional theory in computational chemistry: an overview and extensive assessment of 200 density functionals.," *Molecular Physics.,* vol. 115, no. 19, pp. 2315-2372., 2017.

[22] Q. Liao, J. Chen, L. Zhou and e. al., " Bandgap Engineering of Lead-Free Double Perovskite Cs2AgInCl6 Nanocrystals via Cu2+-Doping.," *Journal of Physical Chemistry Letters. ,* vol. 11, no. 19, pp. 8392-8398, 2020.

[23] K. Hossain, M. Z. Hasan and M. L. Ali, "Narrowing bandgap and enhanced mechanical and optoelectronic properties of perovskite halides: Effects of metal doping.," *AIP Advances,* vol. 11, no. 1, p. 015052, 2021.

[24] M. Z. Rahaman and A. Akther Hossain, "Effect of metal doping on the visible light absorption, electronic structure and mechanical properties of non-toxic metal halide CsGeCl3.," *RSC Advances.,* vol. 8, no. 58, pp. 33010-33018, 2018.

[25] S. Amraoui, A. Feraoun and M. Kerouad, "Performance analysis of lead-free halide double perovskite-based photovoltaic devices for solar cell conception.," *Journal of Alloys and Compounds. ,* vol. 166509, July 2022.

[26] G. Nazir, S. Lee, H. L. Jong and e. al., "Stabilization of Perovskite Solar Cells: Recent Developments and Future Perspectives.," *Advanced Materials. ,* vol. 34, no. 50, 2022.

[27] T. Yang, L. Chu., T. Zhang and e. al., "Thermally stable near-infrared emission from a double perovskite K2LiScF6:Cr3+ phosphor for light-emitting diodes.," *Journal of Alloys and Compounds. ,* vol. 965, pp. 171336-171336, 2023.

[28] D. K. Paul and A. A. Hossain, "A comprehensive DFT + U investigation of electrical, optical, and structural properties of doped CsSnCl3 Perovskite: Unveiling optoelectronic potential.," *Computational Materials Science. ,* vol. 231, pp. 112585-112585, 2024.

[29] J. Islam and A. Hossain, "Narrowing band gap and enhanced visible-light absorption of metal-doped non-toxic CsSnCl3 metal halides for potential optoelectronic applications.," *RSC Advances.,* vol. 10, no. 13, pp. 7817-7827, 2020.

[30] M. R. Filip, S. Hillman, A. A. Haghighirad and e. al., "Band Gaps of the Lead-Free Halide Double Perovskites Cs2BiAgCl6 and Cs2BiAgBr6 from Theory and Experiment.," *The Journal of Physical Chemistry Letters.,* vol. 7, no. 13, pp. 2579-2585, 2016.

[31] Y. Chrafih, M. Al-Hattab and K. Rahmani, "'Thermodynamic, optical, and morphological studies of the Cs2AgBiX6 double perovskites (X = Cl, Br, and I): Insights from DFT study',," *Journal of Alloys and Compounds,,* vol. 960, pp. 170650-170650, 2023.

[32] Y. Saeed, B. Amin, H. Khalil and e. al, "Cs2NaGaBr6: a new lead-free and direct band gap halide double perovskite.," *RSC Advances,* vol. 10, no. 34, pp. 20196-20196, 2020.

[33] M. Nabi and D. C. Gupta, "Potential lead-free small band gap halide double perovskites Cs2CuMCl6 (M = Sb, Bi) for green technology.," *Scientific Reports.,* vol. 11, no. 1, 2021.

[34] D. Metin and N. Gaston, "Internal and external pressure in cubic perovskites: electronic structure effects and systematic accuracy from first principles.," *Electron. Struct.,* vol. 1, p. 035001, 2019.

[35] Y. Ying, X. Luo and H. Huang, "Pressure-induced topological nontrivial phase and tunable optical properties in all-inorganic halide perovskites.," *J. Phys. Chem. C,* vol. 122, pp. 17718-17725, 2018.

[36] K. Momma and F. Izumi, "VESTA 3 for three-dimensional visualization of crystal, volumetric and morphology data," *Journal of Applied Crystallography,* vol. 44, pp. 1272-1276, 2011.

[37] J. Barrett, S. Bird, J. Donaldson and S. Donaldson, "The Mössbauer effect in tin (II) compounds. Part XI. The spectra of cubic trihalogenostannates (II)," *J. Chem. Soc. A: Inorg., Phys., Theor.,* pp. 3105-3108, 1971.

[38] M. Segall, P. Lindan, M. Probert and e. al., "First-principles simulation: ideas, illustrations and the CASTEP code.," *J. Condens. Matter Phys.,* vol. 14, p. 2717, 2002.

[39] C. Ambrosch-Draxl and R. Abt, The calculation of optical properties within WIEN97., ICTP Lecture Notes., 1998.

[40] P. Yu and M. Cardona, Fundamentals of semiconductors: physics and materials properties., Berlin: Springer, 1996.

[41] M. Fox, Optical properties of solids., New York: Oxford University Press, 2001.

[42] A. Delin, O. Eriksson, R. Ahuja and et al., "Optical properties of the group-IVB refractory metal compounds.," *Phys. Rev. B,* vol. 54, p. 1673, 1996.

[43] D. S. M. a. C. C. Hamann, "Norm-conserving pseudopotentials.," *Phys. Rev. Lett.,* vol. 43, p. 1494, 1979.

[44] A. Hossain, "Synthesis and Characterization of FeCo Alloy Encapsulated with CoFe2O4 Nanoparticles Using Sol-gel Route and First Principles Study," February 2017. [Online]. Available: DOI: 10.13140/RG.2.2.26305.30566.

[45] W. Kohn and L. Sham, "Self-consistent equations including exchange and correlation effects.," *Phys. Rev.,* vol. 140, p. 1133, 1965.

[46] Y. Wu, G. Xiang, M. Zhang and e. al, "The effect of uniaxial strain on electronic and optical properties of halide double perovskites Cs2AgXCl6 (X=Sb, Bi): a DFT approach," *Journal of Alloys and Compounds.,* vol. 961, pp. 170995-170995, 2023.

[47] J. P. Connerade, A. Solovyov and E. Surdutovich, "A Review of Quantum Confinement," *AIP,* pp. 1-33, Jan 2010.

[48] G. F. Heidari and D. Velauthapillai, "A Review on Cs-Based Pb-Free Double Halide Perovskites: From Theoretical and Experimental Studies to Doping and Applications.," *Molecules,* vol. 26, no. 7, p. 2010, 2021.

[49] T. Sachin, S. R. Rondiya, N. Y. Dzade and e. al., "Experimental and Theoretical Investigation of the Structural and Opto-electronic Properties of Fe-Doped Lead-Free Cs2AgBiCl6 Double Perovskite.," *Chemistry - A European Journal.,* vol. 27, no. 26, pp. 7408-7417, 2021.

[50] W. Sha , X. Ren, L. Chen and W. Choy, " The efficiency limit of CH3NH3PbI3 perovskite solar cells.," *Applied Physics Letters.,* vol. 106, no. 22, p. 221104, 2015.

[51] B. Diouf, A. Muley and . P. Ramchandra, " Issues, Challenges, and Future Perspectives of Perovskites for Energy Conversion Applications.," *Energies,* vol. 16, no. 18, pp. 6498-6498, 2023.

[52] P. Hohenberg and W. Kohn, "Density functional theory (DFT)," *Phys. Rev B,* vol. 136, p. 864, 1964.

[53] M. A. Hadi, "First-principles Study of Superconducting MAX Phases,," M.Phil. Thesis, 2015.

[54] G. Ackland, "Embrittlement and the bistable crystal structure of zirconium hydride," *Phys. Rev. Lett.,* vol. 80, p. 2233, 1998.

[55] R. Hill, "The elastic behavior of a crystalline aggregate," *Proceedings of the Physical Society of London Series A.,* vol. 65, pp. 349-354, 1952.

[56] V. Milman and M. Warren, "Elastic properties of TiB2 and MgB2.," *J. Phys. Condens. Matter,* vol. 13, p. 5585, 2001.

[57] E. Schrödinger, "Quantisierung als eigenwertproblem.," *Ann. Phys.,* vol. 385, pp. 437-490, 1926.

[58] D. Hartree, "The wave mechanics of an atom with a non-coulomb central field. Part II. Some results and discussion.," *Math. Proc. Cambridge Philos. Soc.,* vol. 24, pp. 111-132, 1928.

[59] C. Roothaan, "New developments in molecular orbital theory.," *Rev. Mod. Phys.,* vol. 23, no. 2, p. 69, 1951.

[60] F. a. P. G. Kutzler, "First-row diatomics: Calculation of the geometry and energetics using self-consistent gradient-functional approximations.," *Phys. Rev. B,* vol. 45, p. 3236, 1992.

[61] D. Vanderbilt, "Soft self-consistent pseudopotentials in a generalized eigenvalue formalism.," *Phys. Rev. B,* vol. 41, p. 7892, 1990.

[63] Dholon Kumar Paul, Wajiha Tarannum Chaudhry, SM Naimul Mamun, M.L. Rahman, AFM Yusuf Haider and Firoze H. Haque, "Impact of doping and hydrostatic pressure on structural, electronic, optical, and mechanical properties of novel double halide perovskite Cs2LiGaBr6," *ChemPhysMater,* no. https://doi.org/10.1016/j.chphma.2024.06.006, June 2024.

Peer Reviewed Journal

"Impact of doping and hydrostatic pressure on structural, electronic, optical, and mechanical properties of novel double halide perovskite Cs2LiGaBr6,"

Dholon Kumar Paul, **Wajiha Tarannum Chaudhry**, SM Naimul Mamun, M.L. Rahman, AFM Yusuf Haider and Firoze H. Haque.

ChemPhysMater; 26 June 2024.

doi: https://doi.org/10.1016/j.chphma.2024.06.006